nature

SUPPLEMENTARY INFORMATION

https://doi.org/10.1038/s41586-018-0869-5

In the format provided by the authors and unedited.

Atomically dispersed iron hydroxide anchored on Pt for preferential oxidation of CO in H_2

Lina Cao[1,3,7], Wei Liu[2,7], Qiquan Luo[1,3,7], Ruoting Yin[1,3], Bing Wang[1,3], Jonas Weissenrieder[4], Markus Soldemo[4], Huan Yan[1,3], Yue Lin[1], Zhihu Sun[2], Chao Ma[1], Wenhua Zhang[1], Si Chen[1,3], Hengwei Wang[1,3], Qiaoqiao Guan[1,3], Tao Yao[2], Shiqiang Wei[2]*, Jinlong Yang[1,3,5]* & Junling Lu[1,3,5,6]*

[1]Hefei National Laboratory for Physical Sciences at the Microscale, University of Science and Technology of China, Hefei, China. [2]National Synchrotron Radiation Laboratory, University of Science and Technology of China, Hefei, China. [3]Department of Chemical Physics, University of Science and Technology of China, Hefei, China. [4]School of Engineering Sciences, KTH Royal Institute of Technology, Stockholm, Sweden. [5]Collaborative Innovation Center of Chemistry for Energy Materials (*i*ChEM), University of Science and Technology of China, Hefei, China. [6]CAS Key Laboratory of Materials for Energy Conversion, University of Science and Technology of China, Hefei, China. [7]These authors contributed equally: Lina Cao, Wei Liu, Qiquan Luo. *e-mail: junling@ustc.edu.cn; sqwei@ustc.edu.cn; jlyang@ustc.edu.cn

Atomically dispersed iron hydroxide anchored on Pt for preferential oxidation of CO in H_2

Lina Cao,[1,3,†] Wei Liu,[2,†] Qiquan Luo,[1,3,†] Ruoting Yin,[1,3] Bing Wang,[1,3] Jonas Weissenrieder,[4] Markus Soldemo,[4] Huan Yan,[1,3] Yue Lin,[1] Zhihu Sun,[2] Chao Ma,[1] Wenhua Zhang,[1] Si Chen,[1] Hengwei Wang,[1,3] Qiaoqiao Guan,[1,3] Tao Yao,[2] Shiqiang Wei,[2,*] Jinlong Yang,[1,3,6,*] Junling Lu[1,3,5,6*]

[†]These authors contributed equally to this work.

To whom correspondence should be addressed: E-mail: junling@ustc.edu.cn (J.L.L.), sqwei@ustc.edu.cn (S.Q.W.), and jlyang@ustc.edu.cn (J.L.Y.)

Methods

Materials. Trimethyl(methylcyclopentadienyl)platinum(IV) ($MeCpPtMe_3$) was purchased from Strem Chemicals. The silica support (BET surface area 300 m^2/g) and ferrocene ($FeCp_2$) were both bought from Sigma Aldrich. Ultrahigh purity N_2 (99.999%), O_2 (99.999%), H_2 (99.999%), He (99.999%), CO_2 (99.999%) and the mixture of 10% CO in He were all provided by Nanjing Special Gases. All chemicals were used as received without further purification. Reference samples of Fe_2O_3 (99.9995%), FeOOH and FeO (99.5%) were purchased from Sinopharm Chemical Reagent Co. Ltd. For the XPS-measurements, the following gas mixtures from Air Liquide were used: 10 (± 1)% O_2 in Argon, 10 (± 1)% H_2 in Argon, and 5 (± 0.25)% H_2 + 1 (± 0.05)% CO + 0.5 (±0.025)% O_2 in Argon.

Pt ALD: Synthesis of Pt/SiO_2 catalyst. Pt ALD was carried out on the silica support to synthesize the Pt/SiO_2 catalyst in a viscous flow ALD reactor (GEMSTAR-6^{TM}, Benchtop ALD, Arradiance) using $MeCpPtMe_3$ and ultrahigh purity O_2 (99.9999%) at 523 K. Ultrahigh purity N_2 (99.999%) was used as a carrier gas at a flow rate of 200 ml/min. The $MeCpPtMe_3$ precursor container was heated to 343 K to achieve a sufficient vapor pressure. The ALD chamber was heated to 523 K and the inlet manifold was held at 383 K to avoid precursor condensation on the inner walls. The timing sequence was 600, 300, 160, and 300 seconds for the $MeCpPtMe_3$ exposure, N_2 purge, O_2 exposure, and N_2 purge, respectively (600-300-160-300). Pt ALD was performed for two ALD cycles.

Pt ALD: Synthesis of a Pt film model catalyst. Pt ALD was also carried out on silicon wafers for 300 cycles to grow a thick Pt film at 573 K with the timing sequence of (5-5-5-5). The Pt film thickness was about 15 nm according to the growth rate of Pt ALD (0.05 nm/cycle). This Pt film was taken as a model Pt surface for growing FeO_x ALD.

FeO_x ALD: Synthesis of *x*cFe-Pt/SiO_2 catalysts. FeO_x ALD was carried out on the Pt/SiO_2 catalyst at 393 K using $FeCp_2$ and ultrahigh purity O_2 (99.999%) in the same ALD reactor. The $FeCp_2$ precursor container was heated to 363 K to achieve a sufficient vapor pressure. The ALD chamber was heated to 393 K and the inlet manifold was held at 393 K to avoid precursor condensation on the inner walls. The timing sequence was (300-300-200-300). Different cycles of FeO_x ALD were carried out to obtain a series of the catalysts (denoted as *x*cFe-Pt/SiO_2, here *x* represents the number of ALD cycles). The deposition temperature here was far below the conventional temperature of 623-773 K for FeO_x ALD using the same process to inhibit the growth of FeO_x on the silica gel support[1,2]. As a control experiment, FeO_x ALD was also performed on the bare SiO_2 substrate for different cycles under the same ALD conditions (denoted as *x*cFe/SiO_2).

In order to initiate the growth of FeO_x ALD on the bare SiO_2 substrate, FeO_x ALD was also performed at 563 K for 10 cycles (denoted as 10cFe/SiO_2-563K).

FeO_x ALD: Synthesis of 3cFe-Pt and 10cFe-Pt film model catalysts. FeO_x ALD was also carried out on the thin Pt film model catalyst for 10 cycles at 393 K with the timing sequence of (45-20-30-20). The resulting Pt film coated with either 3 or10 ALD cycles of FeO_x is denoted as 3cFe-Pt film, and 10cFe-Pt film model catalyst, respectively.

Synthesis of Pt/Fe_2O_3 catalyst by wet impregnation method 39.7 mg of tetraammineplatium($Pt(NO_3)_2(NH_3)_4$) was first dissolved in 50 mL deionized water, then stirring for 5 min at room temperature (RT). Next, 500 mg of the alpha-Fe_2O_3 was

slowly added into the $Pt(NO_3)_2(NH_3)_4$ solution , while keeping stirring for 24 h at RT. After that, the mixture was dried at 353 K using oil bath for 3 h. The resulting materials were calcined in 10%O_2/He at the flow rate of 25 ml/min at 373 K for 1 h then at 573 K for another 2 h to get the Pt/Fe_2O_3 catalyst.

Morphology and compositions. Aberration-corrected HAADF-STEM measurements were taken on a JEM-ARM200F instrument (University of Science and Technology of China) at 200 keV. Meanwhile, energy-dispersive X-ray (EDX) spectroscopy was also collected on the same equipment. The Pt and Fe loadings of the *x*cFe-Pt/SiO_2 catalysts were analyzed by an inductively coupled plasma atomic emission spectrometer (ICP-AES); therein all samples were dissolved in hot aqua regia.

In situ X-ray absorption fine structure (XAFS) spectroscopy. In situ XAFS measurements at Fe K-edge (7112 eV) and Pt L_3-edge (11564 eV) were performed with the Si(111) monochromator at the 1W1B beamline of Beijing Synchrotron Radiation Facility (BSRF), China and the BL14W1 beamline of the Shanghai Synchrotron Radiation Facility (SSRF), China. The storage ring of BSRF worked at 2.5 GeV with a maximum current of 250 mA, and the storage ring of SSRF worked at 3.5 GeV with a maximum current of 210 mA. The XAFS spectra at Fe K-edge and Pt L_3 edge were recorded in fluorescence and transmission mode, respectively, considering the loadings of Fe and Pt. The 1cFe-Pt/SiO_2 catalyst was first pressed into a sample pellet and was then loaded into a home-made quartz reaction cell, where Kapton foil was used as the X-ray window material. This quartz reaction cell can be heated to 773 K with external heating. A K-type thermocouple, protected by a closed-end quartz tube, was located near the sample pellet to measure the sample temperature.

After loading into the reaction cell, the pristine 1cFe-Pt/SiO_2 sample was purged in helium at RT for 30 min, and a XAFS spectrum was then recorded (1cFe-Pt/SiO_2-O). After that, the sample was reduced in 10% H_2 in He at room temperature for 30 min, and a XAFS spectrum was recorded (1cFe-Pt/SiO_2-R). Next, the sample was exposed to the PROX reaction stream of 1% CO, 0.5% O_2, and 48% H_2 in helium at RT for 30 min, and the XAFS spectrum of 1cFe-Pt/SiO_2 catalyst under PROX conditions was taken (1cFe-Pt/SiO_2-P). After that, the sample was further reduced in 10% H_2 in He at 473 K for 30 min and a XAFS spectrum was recorded (1cFe-Pt/SiO_2-R(473K)) after cooling the sample to near RT. Finally, the sample was exposed to the PROX reaction stream at 473 K for another 30 min and a XAFS spectrum was recorded (1cFe-Pt/SiO_2-P(473K)) after cooling the sample to near RT. Moreover, the *x*cFe-Pt/SiO_2 samples (*x* = 0.4, 3, and 10) were pre-treated according to the same procedure with 1cFe-Pt/SiO_2, in the sequence of purging in helium at RT, reduction at RT, and at 473 K. The corresponding XAFS data was assigned to be *x*cFe-Pt/SiO_2-O, *x*cFe-Pt/SiO_2-R, and *x*cFe-Pt/SiO_2-R(473K), respectively.

X-ray photoelectron spectroscopy (XPS). XPS measurements was performed at the beamline I311 at the MAX-lab (Lund, Sweden)[3]. The O 1s spectra were recorded using 640 and 870 eV photon energies and the binding energy was calibrated relative to the Fermi level. The ambient pressure cell was in direct connection with the preparation chamber of the beamline endstation, allowing for direct sample transfer without exposure to ambient air after pretreating samples at relevant reaction conditions.

In order to investigate the oxygen species in the deposited iron oxide moiety on Pt nanoparticle surfaces, the 3cFe-Pt and 10cFe-Pt film model catalysts were investigated. Here a thin Pt film model catalyst was used to isolate the oxygen species from the SiO_2

support in the real catalysts of *x*cFe-Pt/SiO_2 during XPS studies. The 3cFe-Pt and 10cFe-Pt film model catalysts were first calcined in 10% O_2 in Ar at 473 K for 30 min, then reduced in 10% H_2 in Ar at 473 K for 30 min, and exposed to the PROX reaction gas at room temperature for 60 min, respectively. In this case, the PROX reaction gas consists of 1% CO, 0.5% O_2, 5% H_2, balanced in Ar. After each step, XPS spectra in the O1s region were recorded.

Scanning tunneling microscopy (STM). The morphology and the growth of FeO_x ALD film on Pt(111) surface was also investigated using STM (UNISOKU LT-SPM-1400) at a base pressure of 8×10^{-11} mbar. The Pt single crystal was cleaned by cycles of Ar+ sputtering and a short time annealing to 1000 K[4]. $FeCp_2$ was introduced to the vacuum chamber through a leak valve for ~ 100 L, while the clean Pt(111) surface was maintained at 393 K to simulate the FeO_x ALD condition. After exposing to $FeCp_2$, the Pt crystal was transferred to the analysis chamber for STM measurements at 78 K. Next, the sample was transferred back to the preparation chamber, and was exposed to 1×10^{-6} mbar O_2 for 30 min at 473 K, followed by another annealing step by closing the O_2 source at 473 K for another 30 min to finish one FeO_x ALD cycle. STM images were taken again on this sample.

Catalytic activity test. The PROX reactions were carried out in a fixed-bed U-shape quartz tube flow reactor system with an inner diameter of 10 mm at atmospheric pressure. 100 mg *x*cFe-Pt/SiO_2 catalyst was diluted with 1 g fine quartz chips to avoid catalytic "hot spots". Moreover, a K-type thermocouple, protected by a 1/8 inch closed-end quartz tube was placed directly in the catalyst bed to measure the sample temperature. Before the reaction test, the catalyst was calcined in 10% oxygen in helium at a flow rate of 25 ml min^{-1} at 473 K for 1 h, followed by a reduction step by 10% hydrogen in helium for another 2 h, and an activation step by exposing the catalyst to the PROX reaction stream of 1% CO, 0.5% O_2, and 48% H_2 in helium at a flow rate of 60 ml/min at 473 K for 20 min. The flow rate of the pretreatment gases was controlled by mass flow controllers (Beijing Seven Star Instruments). Next, the PROX reaction was conducted in a temperature range of 180-473 K, where the reaction gas feed consisted of 1% CO, 0.5-1% O_2, and 48% H_2 balanced in helium at a total flow rate of 60 ml/min. The products were analyzed by an online gas chromatography (Agilent 7890A) equipped with a TCD detector and two capillary columns (HP-MOLESIEVE, 30 m × 0.53 mm and PoraPLOT U columns (27.5 m × 0.53 mm). The products detected from these two columns were normalized for quantification using standards gases provided by Nanjing Special Gases. CO conversion and CO selectivity were calculated using the following equations:

$$\text{CO conversion (\%)} = \frac{[\text{CO}]_{in} - [\text{CO}]_{out}}{[\text{CO}]_{in}} \times 100$$

$$\text{CO selectivity (\%)} = \left\{0.5 \times \frac{[\text{CO}]_{in} - [\text{CO}]_{out}}{[\text{O}_2]_{in} - [\text{O}_2]_{out}}\right\} \times 100$$

$[CO]_{in}$, $[CO]_{out}$, $[O_2]_{in}$, and $[O_2]_{out}$, are the concentration of CO and O_2 at the inlet and outlet of reactor, respectively.

Kinetic measurements were performed in the same fixed-bed reactor. For the measurement of mass specific rates and activation energy, the amounts of catalysts were reduced to ensure the CO conversion below 20%. The initial CO conversions after stabilizing in the reaction gas for 20 minutes used for calculations of the specific rates.

Computational methods and models. All calculations were done using the plane-wave spin-polarized periodic density functional method (DFT) in the Vienna *ab initio*

simulation package (VASP)[5,6]. The electron-ion interaction was described with the projector augmented wave (PAW) method[7,8]. The electron exchange and correlation energy was treated within the vdW-DF optimized Becke88 functional (optB88-vdW) [9,10]. The cut-off energy was set up to 500 eV. The force convergence was set to be lower than 0.03 eV/Å, and the total energy convergence was set to be smaller than 10^{-5} eV. Electron smearing of σ = 0.1 eV was used following the the Gaussian scheme. Brillouin zone sampling was employed using a Monkhorst-Pack grid[11]. The nudged elastic band (NEB) method was used to locate the transition states of the hydrogenation reactions[12]. The computed vibrational frequencies were used to characterize a minimum state without imaginary frequencies or an authentic transition state with only one imaginary frequency. The calculated crystal lattice parameter of Pt is 3.96 Å, and it is very close to experimental value of 3.91 Å. The Pt(100) and Pt(111) were modelled by four-layer periodic slab with (3 × 3) supercell; and top two layers were relaxed and fixed two bottom layers in its bulk distances. The vacuum slab was set up to 15 Å (Supplementary Fig. 34).

The binding energy of O 1s orbital was calculated as the energy difference between the ground state and the core-excited state which was simulated by substituting the excited oxygen atom with fluorine atom[13]. And the binding energy of chemisorbed oxygen on Pt surface was set as the reference energy of 529.7 eV, since it is well documented[14]. In our calculations, an extra atomic oxygen atom was put on the Pt(100) or Pt(111) surface and far away the $Fe_1O_xH_y$ moiety.

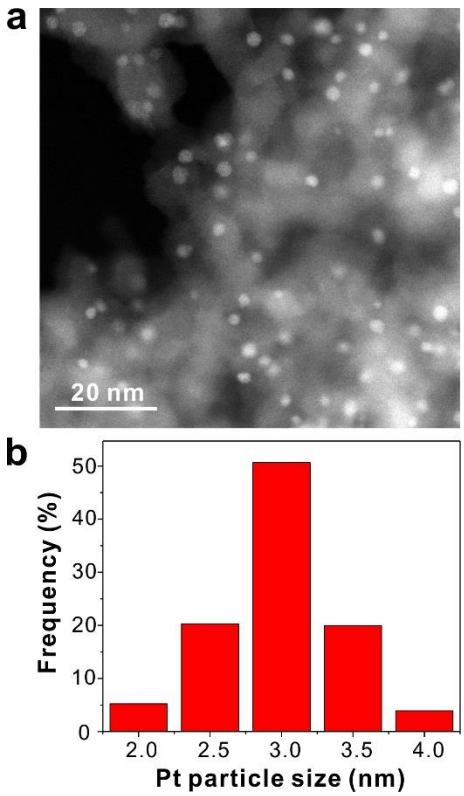

Supplementary Figure 1 | Morphology of the Pt/SiO_2 catalyst. a, a representative STEM image of the Pt/SiO_2 catalyst. **b,** the Pt particle size distribution.

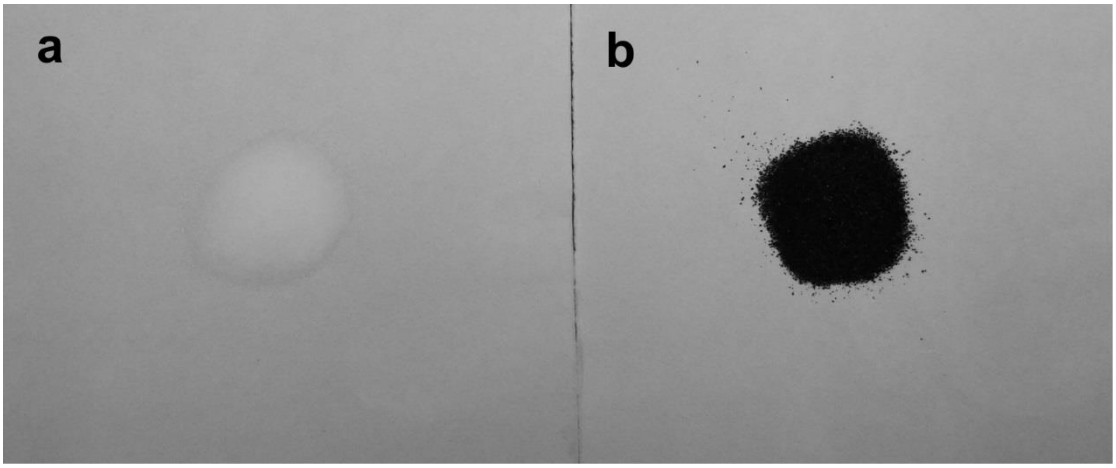

Supplementary Figure 2 | Photographs of the samples after depositing 10 cycles of FeO_x on the bare SiO_2 substrate at 393 K (a) and 563 K (b), respectively. Compared to the deposition at 563 K, depositing 10 cycles of FeO_x on the bare SiO_2 substrate at 393 K did not cause any changes in the color of the SiO_2 substrate, strongly suggesting that there was negligible Fe loadings from FeO_x ALD on the blank SiO_2 support at 393 K.

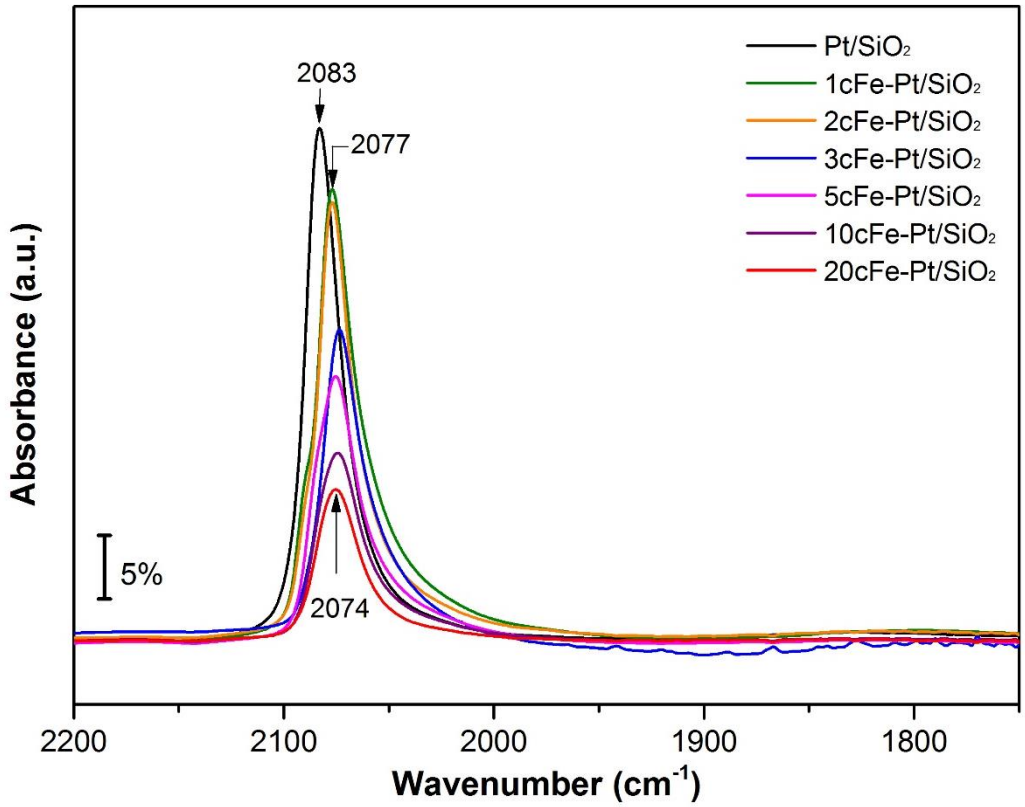

Supplementary Figure 3 | DRIFT spectra of CO chemisorption at 298 K on *x*cFe-Pt/SiO$_2$ catalysts at the CO saturation coverage (*x* = 0, 1, 2, 3, 5, 10, and 20). The gradual decrease in CO peak intensity clearly suggests that the coverages of FeO_x on Pt particles were precisely tuned as increasing ALD cycles.

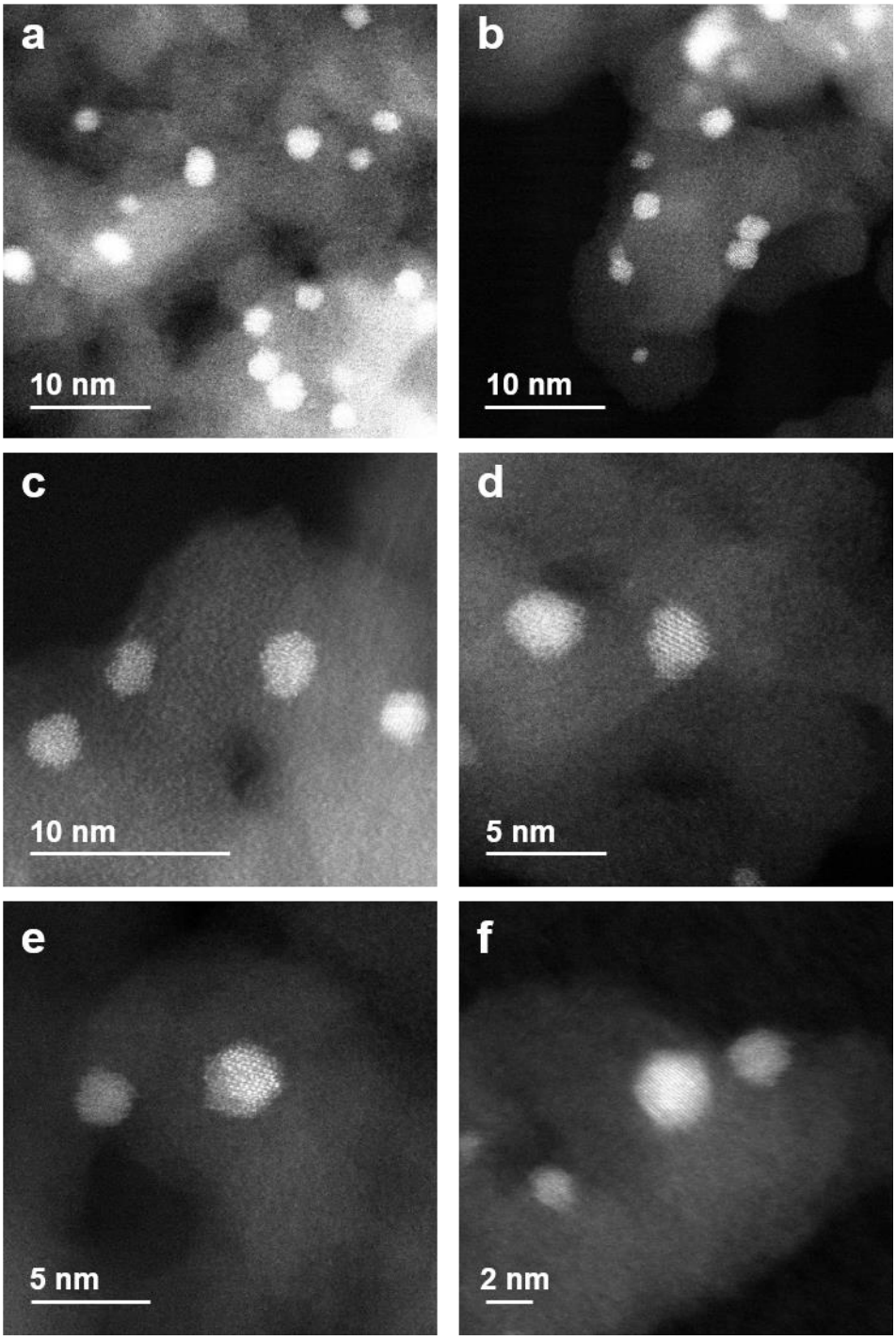

Supplementary Figure 4 | Representative high-resolution HAADF-STEM images of the 10cFe-Pt/SiO_2 catalyst at different locations. There were no any visible ultrafine Pt clusters less than 1 nm size present in our samples.

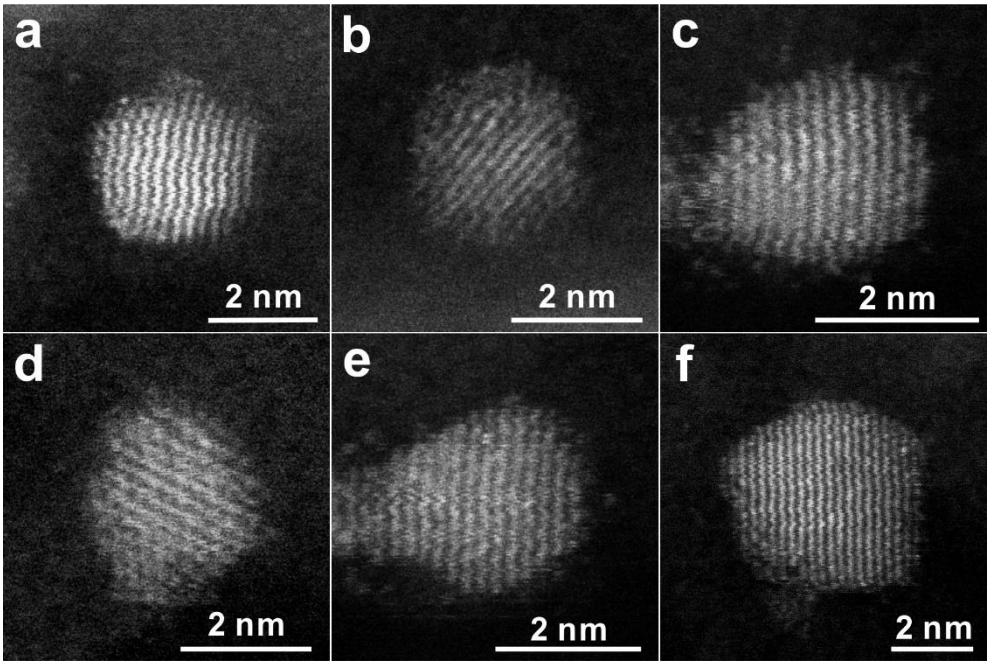

Supplementary Figure 5 | Morphology of the 10cFe-Pt/SiO_2 catalyst. (**a-f**) Aberration-corrected HAADF STEM images of the 10cFe-Pt/SiO_2 catalyst at different locations.

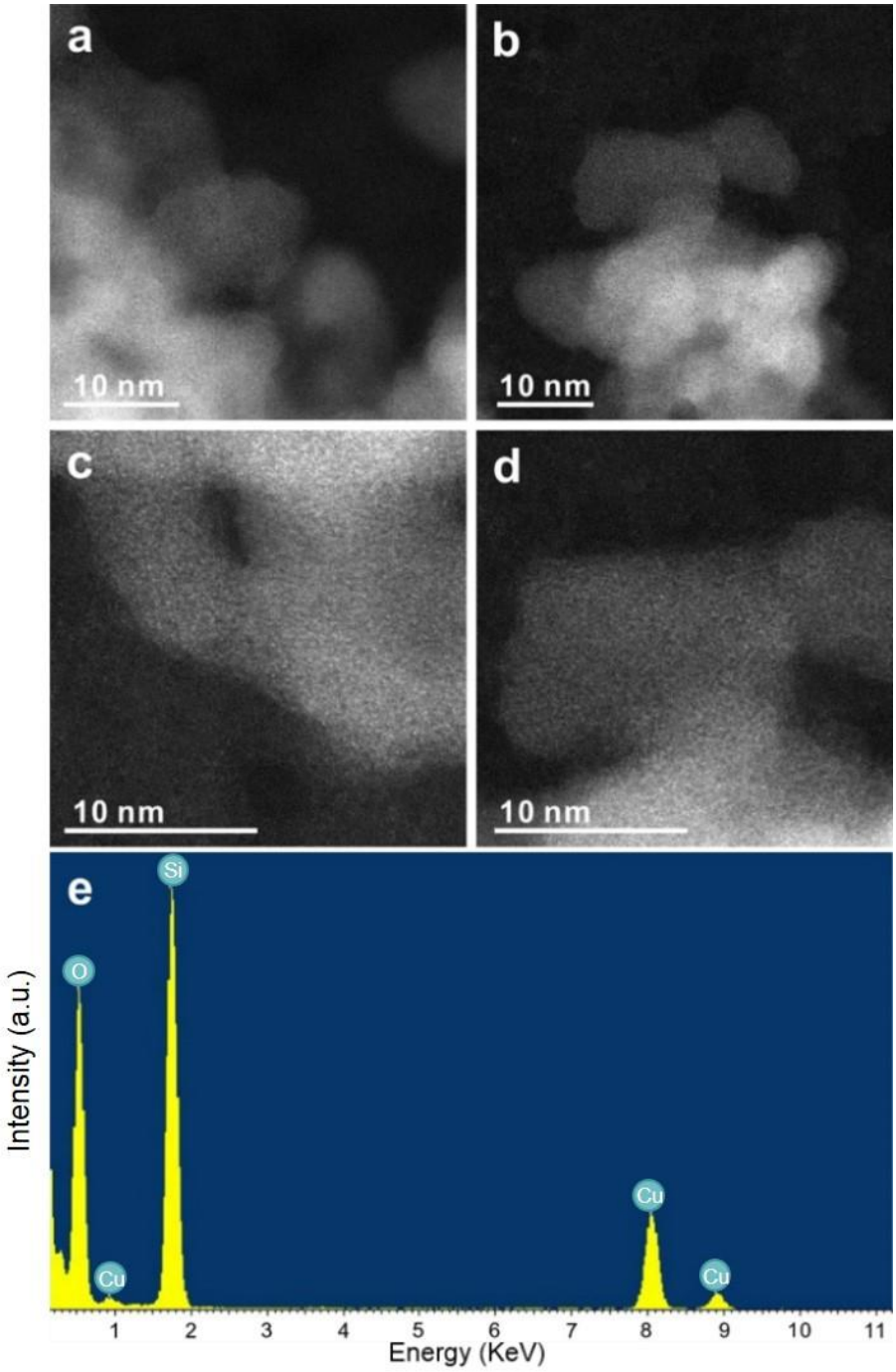

Supplementary Figure 6 | Representative high-resolution HAADF-STEM images of the blank SiO_2 support (a-d), and the corresponding EDS spectrum (e).

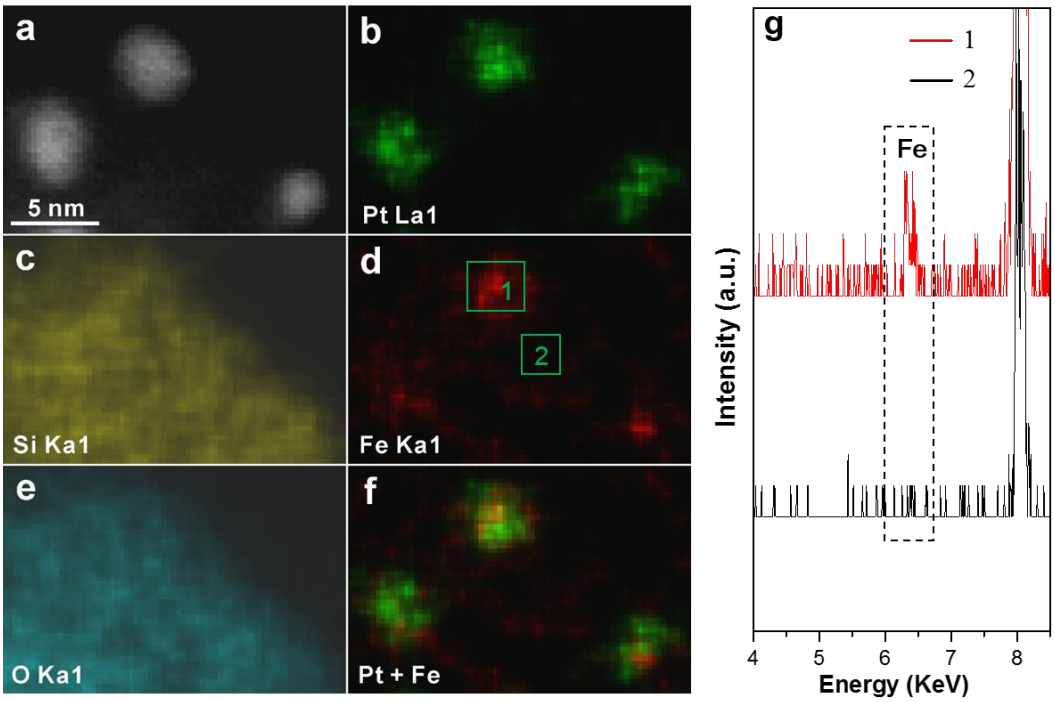

Supplementary Figure 7 | Morphology of the 10cFe-Pt/SiO_2 catalyst. **a,** a HAADF-STEM image of the 10cFe-Pt/SiO_2 catalyst at a different location and the corresponding EDS mapping images: **b,** Pt Lα1; **c,** Si Kα1; **d,** Fe Kα1, **e,** O Kα1; **f,** the reconstructed Pt + Fe composition image, and **g**, individual EDS spectra collected at the particular locations marked and numbered in **d**, indicating the selective deposition of FeO_x on Pt nanoparticles.

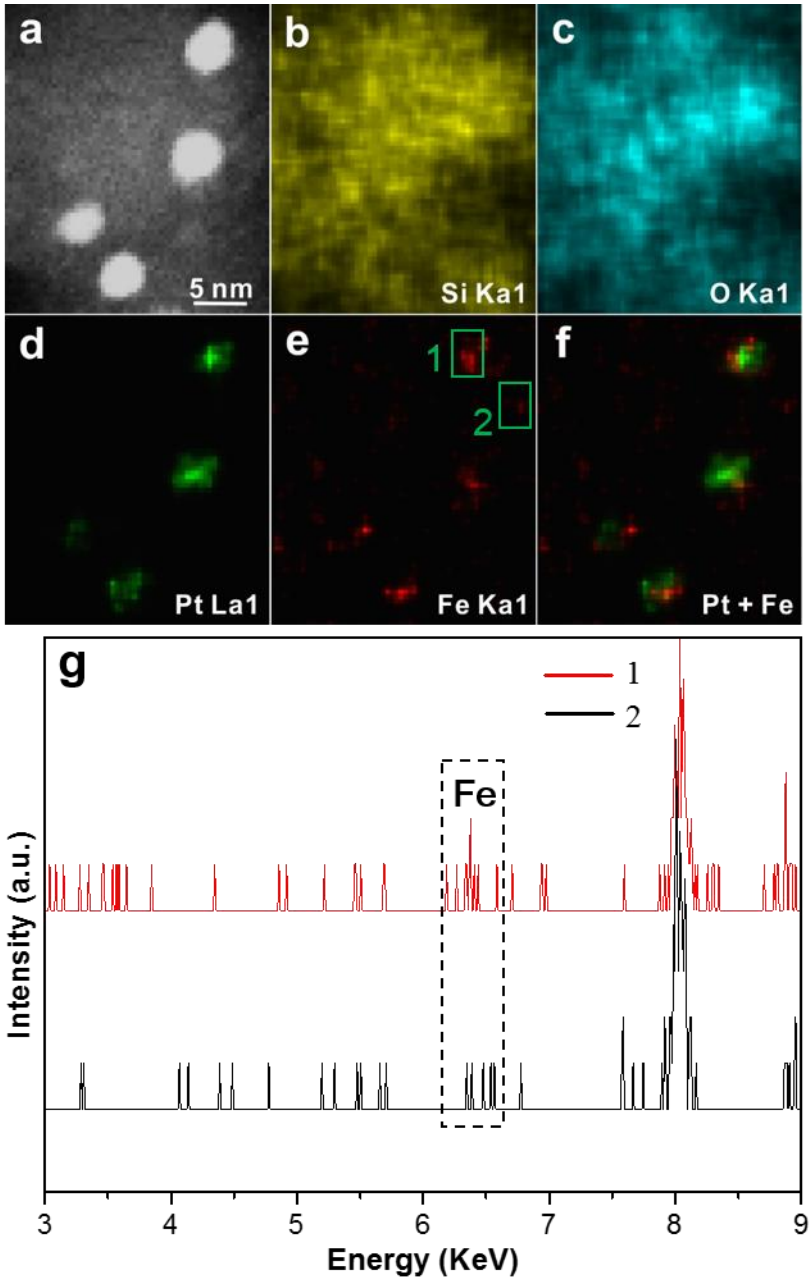

Supplementary Figure 8 | Morphology of the 10cFe-Pt/SiO_2 catalyst. **a,** a HAADF-STEM image of the 10cFe-Pt/SiO_2 catalyst at another location and the corresponding EDS mapping images: **b,** Si Kα1; **c,** O Kα1; **d,** Pt Lα1; **e,** Fe Kα1; **f,** the reconstructed Pt + Fe composition image, and **g**, individual EDS spectra collected at the particular locations marked and numbered in **e**, indicating the selective deposition of FeO_x on Pt nanoparticles.

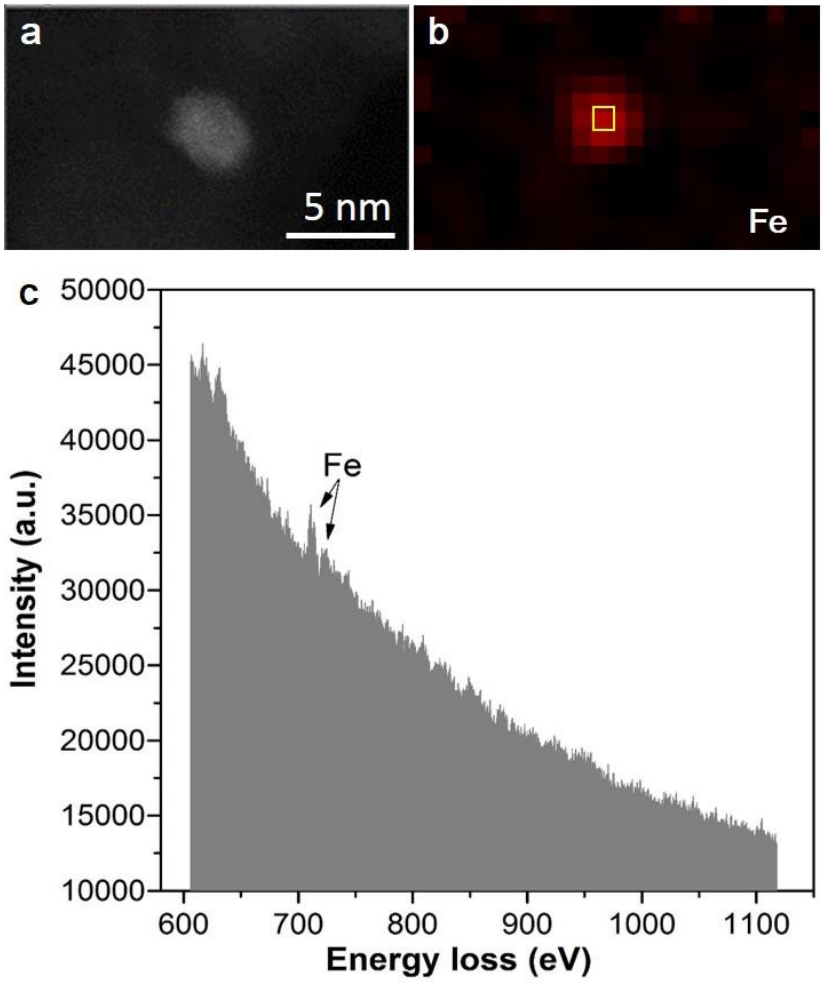

Supplementary Figure 9 | Morphology of the 10cFe-Pt/SiO_2 catalyst. **a,** a HAADF-STEM image of the 10cFe-Pt/SiO_2 catalyst; **b**, the two-dimensional EELS mapping of Fe L-edge in the sample area; **c,** an EELS spectrum of at the location marked by the yellow square in **b**, the Fe L_2- and L_3-edges were highlighted.

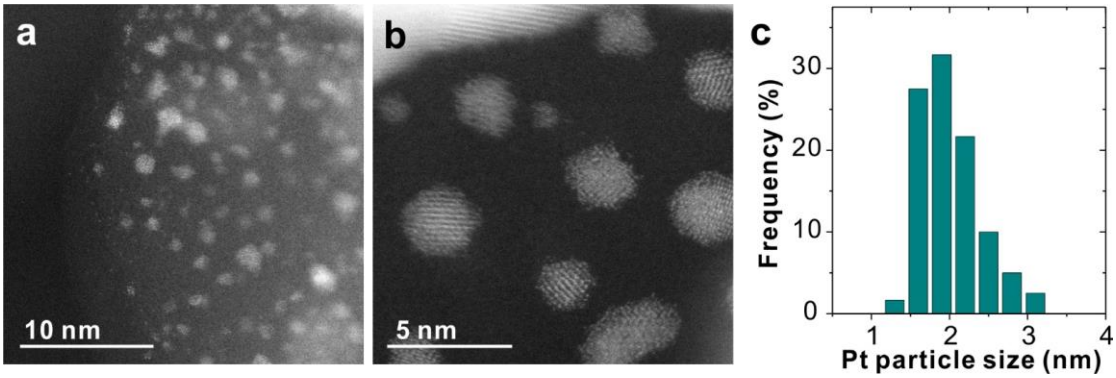

Supplementary Figure 10 | Morphology of the Pt/Fe_2O_3 catalyst. Representative STEM images of the Pt/Fe_2O_3 catalyst at low (**a**) and high (**b**) magnifications. **c,** The Pt particle size distribution.

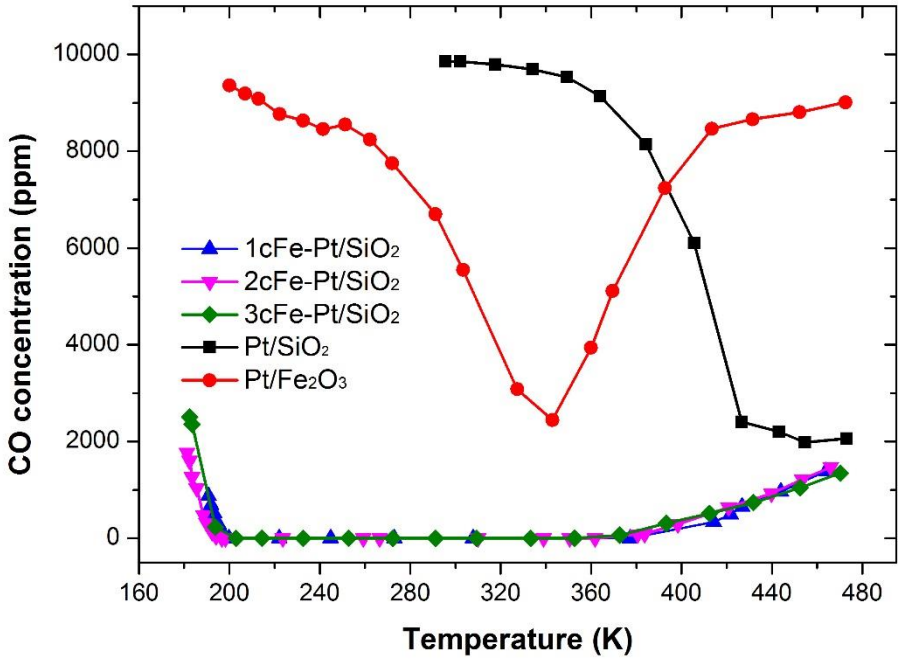

Supplementary Figure 11 | The CO concentration in the reactor outlet as the reaction temperature over *x*cFe-Pt/SiO_2, Pt/SiO_2 and Pt/Fe_2O_3 catalysts in the PROX reaction, here *x* = 1, 2, 3. Reaction conditions: 1% CO, 0.5% O_2, and 48% H_2 balanced in helium; space velocity was 36,000 ml g^{-1} h^{-1}; pressure = 0.1 MPa.

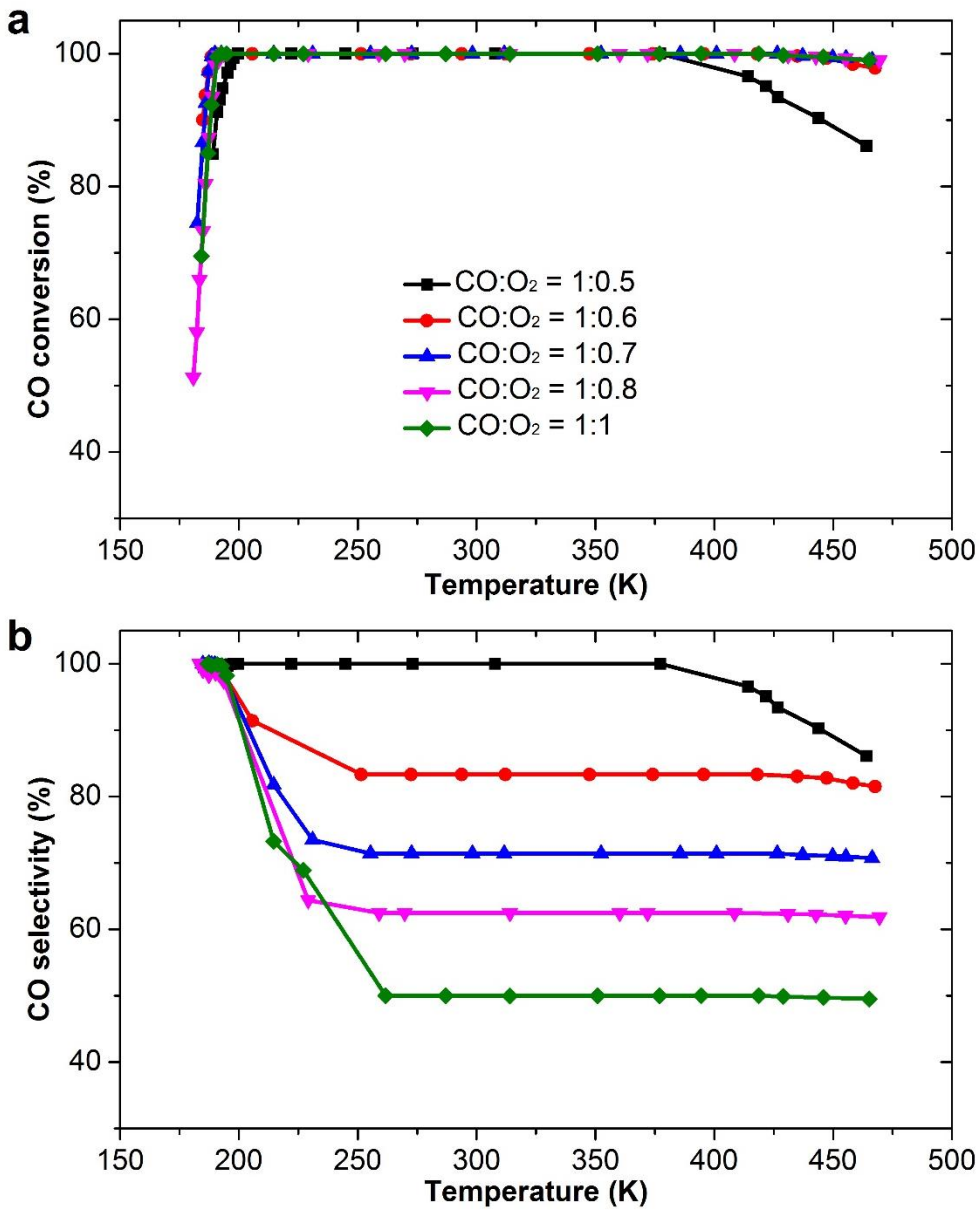

Supplementary Figure 12 | The catalytic performance of the 1cFe-Pt/SiO_2 catalyst in the PROX reaction with different CO:O_2 ratios. **a,** CO conversion; **b**, CO selectivity. Reaction conditions: 1% CO, 0.5-1% O_2, and 48% H_2 balanced in helium; space velocity was 36,000 ml g^{-1} h^{-1}; pressure = 0.1 MPa.

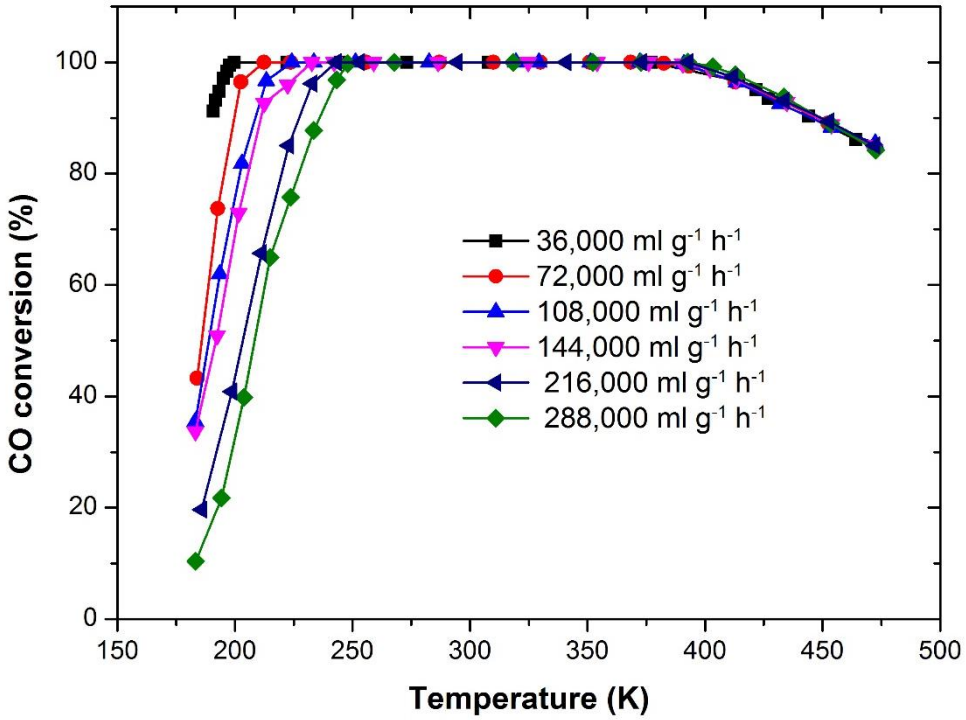

Supplementary Figure 13 | Catalytic performance of 1cFe-Pt/SiO_2 catalyst in the PROX reaction with different space velocities. Reaction conditions: 1% CO, 0.5% O_2, and 48% H_2 balanced in helium; pressure = 0.1 MPa.

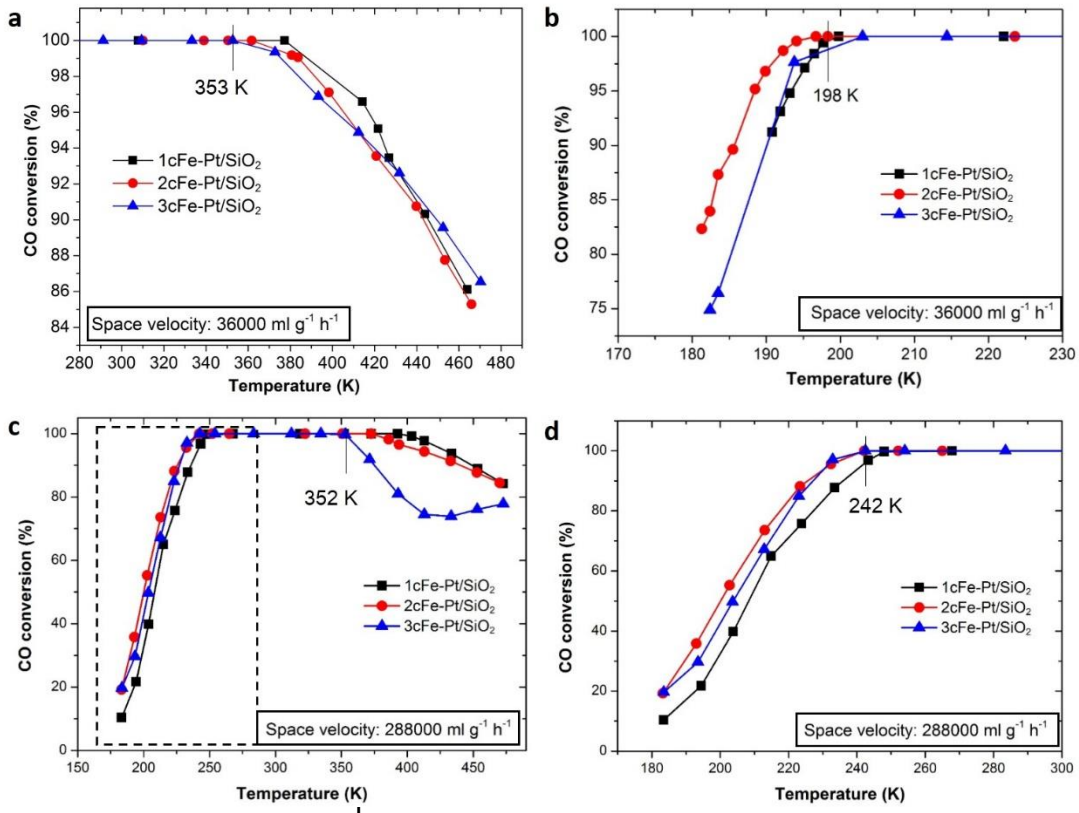

Supplementary Figure 14 | Detailed comparison of the catalytic performances of 1cFe-Pt/SiO_2, 2cFe-Pt/SiO_2 and 3cFe-Pt/SiO_2 catalysts in the PROX reaction with different space velocities. **a,** a closer view of Fig. 2a in the high temperature region with the space velocity of 36,000 ml g^{-1} h^{-1}. **b,** a closer view of Fig. 2a in the low temperature region with the space velocity of 36,000 ml g^{-1} h^{-1}. **c,** their catalytic performances with the space velocity of 288,000 ml g^{-1} h^{-1}. **d,** a closer view of the dash-lined square region in **c**. Reaction conditions: 1% CO, 0.5% O_2, 48% H_2, balanced in helium; pressure = 0.1 MPa.

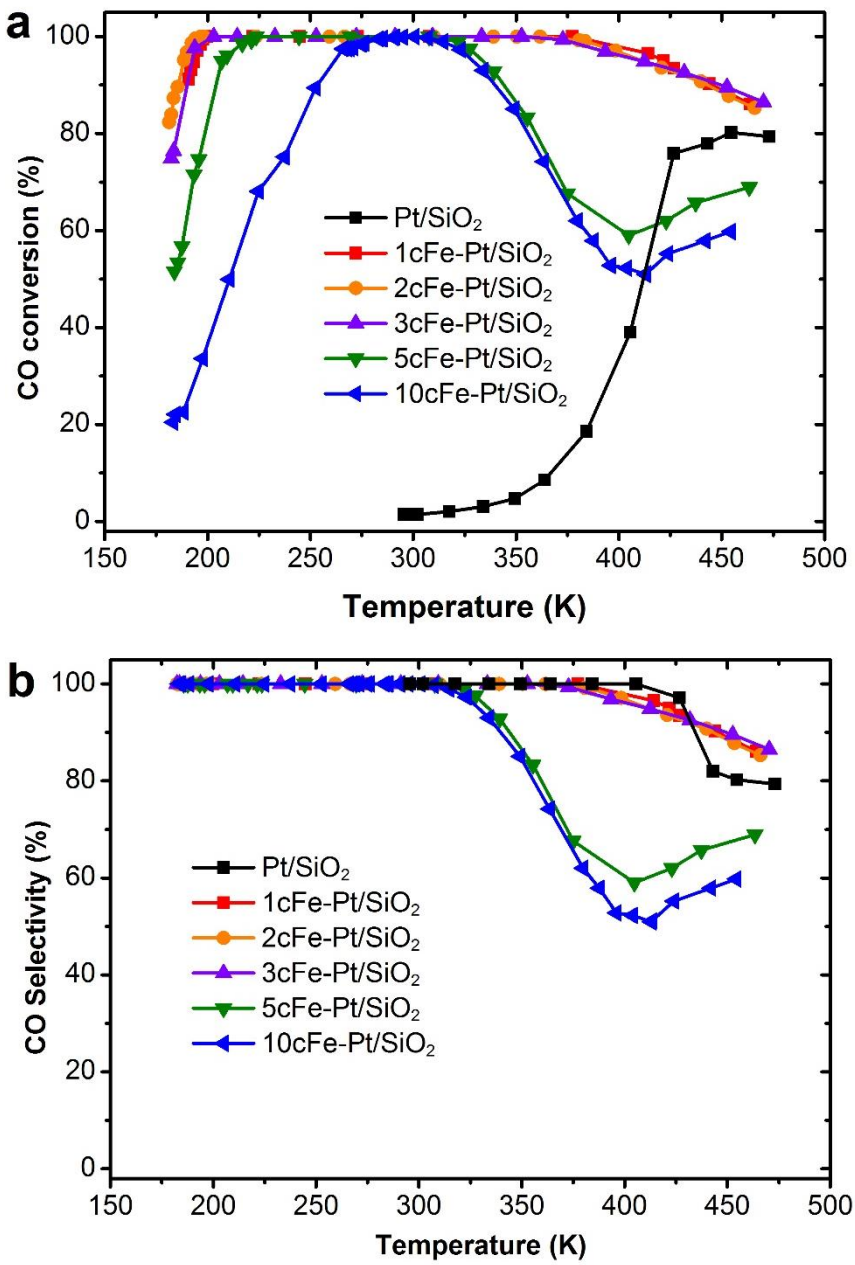

Supplementary Figure 15 | Catalytic performance of *x*cFe-Pt/SiO_2 catalysts in the PROX reaction. a, CO conversion. **b,** CO selectivity. Reaction conditions: 1% CO, 0.5% O_2, and 48% H_2 balanced in helium; space velocity was 36,000 ml g^{-1} h^{-1}; pressure = 0.1 MPa.

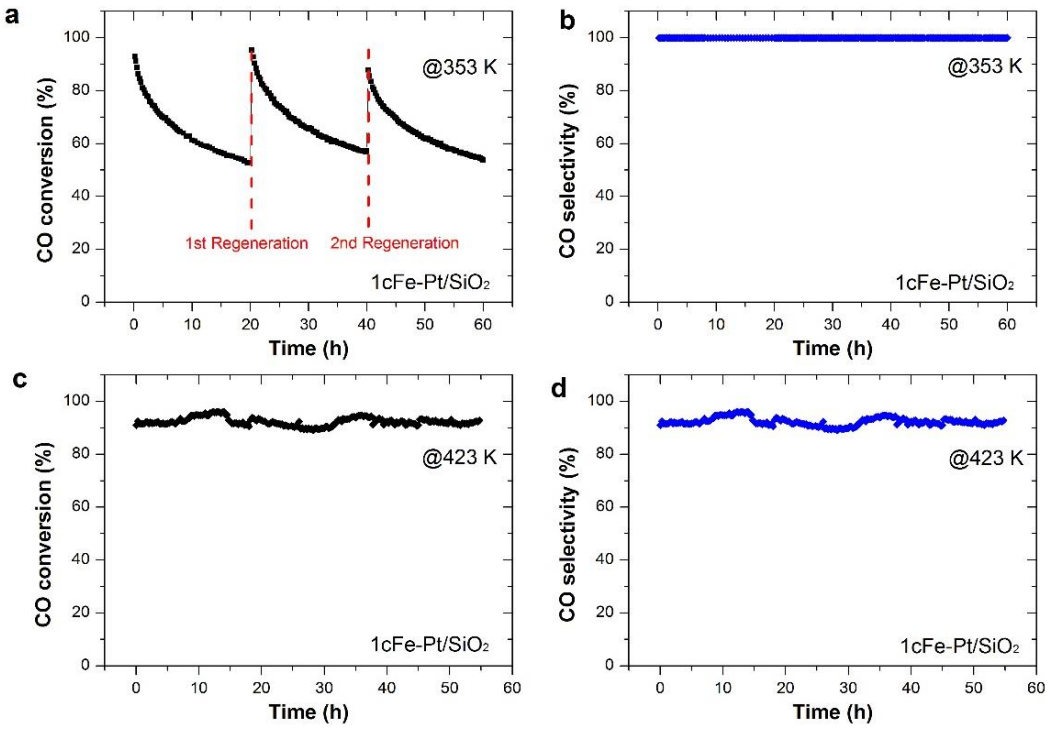

Supplementary Figure 16 | Stability of the 1cFe-Pt/SiO_2 catalyst at 353 (a, b) and 423 K in the PROX reaction (c, d). Reaction conditions for the stability test at 353 K: 1% CO, 0.5% O_2, 48% H_2 and balanced in helium; catalyst,15 mg; space velocity was 480,000 ml g^{-1} h^{-1}; pressure = 0.1 MPa. Reaction conditions for the stability test at 423 K: 1% CO, 0.5% O_2, 48% H_2 and balanced in helium; catalyst, 100 mg; the space velocity was 36,000 ml g^{-1} h^{-1}; pressure = 0.1 MPa.

The stability of 1cFe-Pt/SiO_2.

In order to examine the stability of the 1cFe-Pt/SiO_2 catalyst at a CO conversion below 100% at 353 K, an extremely high space velocitiy of 480,000 ml g^{-1} h^{-1} was used. As shown in Supplementary Fig. 16a and b, a gradual catalyst deactivation was observed. Nonetheless, this catalyst can be fully regenerated by simply increasing the reaction temperature to 473 K in the PROX stream for 30 min. The full recovery of catalyst activity implies that catalyst deactivation is not due to the aggregation of isolated $Fe_1(OH)_3$ species, which otherwise is expected to cause an inreversible catalyst deactivation.

We further tested the catalyst stability at 423 K, which is considerably higher than the temperature (353 K) required for the PEMFC operation. Very interestingly, the 1cFe-Pt/SiO_2 catalyst remained very stable in terms of both activity (~90%) and selectivty (~90%) at 423 K (Supplementary Fig. 16c and d), again suggesting that isolated $Fe_1(OH)_3$ species on Pt are thermally stable. The values of both activity and selectivity of ~90% are consitent with our results shown in Fig. 2a and b.

The structural stability of $Fe_1(OH)_3$ was further confirmed by in situ XAFS measurements of the 1cFe-Pt/SiO_2 catalyst under the PROX reaction conditions at 353 K (Supplementary Fig. 17). Therein, the XAFS spectra for the pristine sample were first recorded during He purge (1cFe-Pt/SiO_2-O) and PROX reaction (1cFe-Pt/SiO_2-P) at RT. After that, the sample was heated up and maintained at 353 K in the PROX reaction for 12 and 24 h, respectively. To record the XAFS spectra in between, the sample was

cooled to RT and then XAFS spectra were recorded immediately. The spectra were denoted as 1cFe-Pt/SiO_2-P-12h and 1cFe-Pt/SiO_2-P-24h, respectively. As shown in Supplementary Fig. 17a, the normalized XANES spectra of 1cFe-Pt/SiO_2-P-12h and 1cFe-Pt/SiO_2-P-24h were almost identical to that of the pristine 1cFe-Pt/SiO_2-P sample in the whole near-edge region; furthermore, the prominent peaks at 1.45 and 2.57 Å in the FT curves ((Supplementary Fig. 17b**)** of 1cFe-Pt/SiO_2-P, assigned to the Fe-O and Fe-Pt coordination, respectively, were also well preserved on 1cFe-Pt/SiO_2-P-12h and 1cFe-Pt/SiO_2-P-24h after the long-term run.

In situ DRIFT spectra also showed that carbonate species on Pt (1690-1695 cm^{-1})[15,16] was not formed even under the PROX reaction for 3.5 h (Supplementary Fig. 18). We also calculated the adsorption of CO_2 on $Fe_1(OH)_3$@Pt(100) and CO_3H on $Fe_1(OH)_2$@Pt(100) to understand whether carbonate species might form on Pt and deactivate the catalyst (Supplementary Fig. 19). By comparing the energy profiles of CO_2 on $Fe_1(OH)_3$@Pt(100) and CO_3H on $Fe_1(OH)_2$@Pt(100), our preliminary results revealed that $Fe_1(OH)_2$+CO_3H is actually 0.38 eV higher in energy than that of $Fe_1(OH)_3$+CO_2. Therefore, the formation of carbonate is thermodynamically unfavorable on our catalyst. In brief, formation of carbonate species on our catalyst may not be the primary reason either from both experimental and theoretical views.

On the other hand, we noticed that the deactivation only occurred at an extremely high space velocitiy of 480,000 ml g^{-1} h^{-1} (the amount of the catalyst was only 15 mg, Supplimentary Fig. 16a). Therefore, we suspect that the trace amount of certain impurities in the reaction gases might have caused the deactivation. Nontheless, the underlying mechanism for the deactivation is still not clearly understood at the moment. Fortunately, it does not affect its practical appliations.

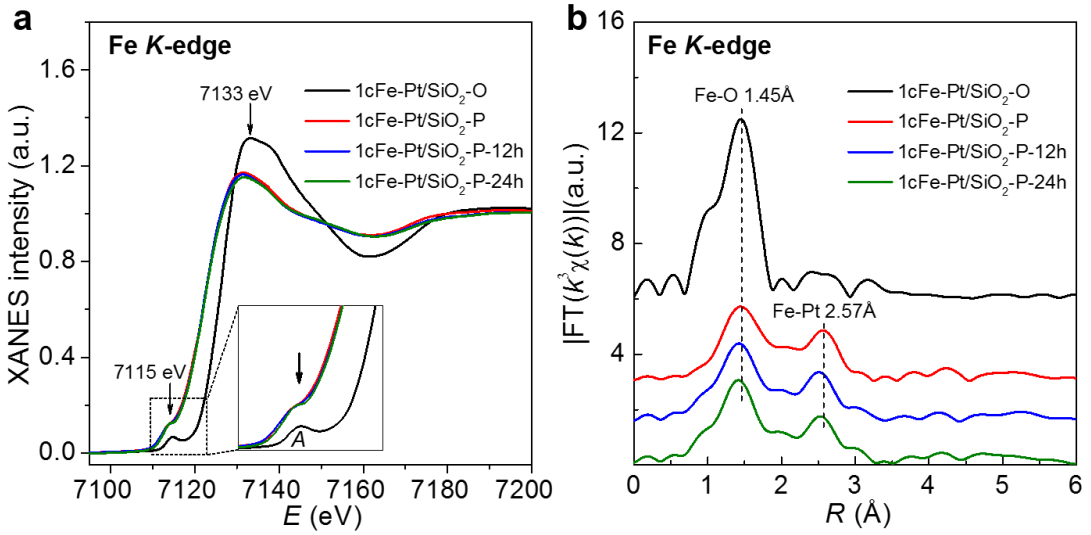

Supplementary Figure 17 | In-situ XAFS measurements of 1cFe-Pt/SiO_2 sample at Fe K-edge. The spectra were recorded first at RT after He purge (1cFe-Pt/SiO_2–O), and PROX reaction (1cFe-Pt/SiO_2–P), and then recorded after RPOX reaction at 353 K for 12 h (1cFe-Pt/SiO_2–P-12h) and RPOX reaction at 353 K for 24 h (1cFe-Pt/SiO_2–P-24h), respectively. **a**, the normalized XANES spectra. The inset shows the magnified pre-edge peak "A" in the dashed line rectangle. **b**, Fourier transforms EXAFS spectra in *R*-space.

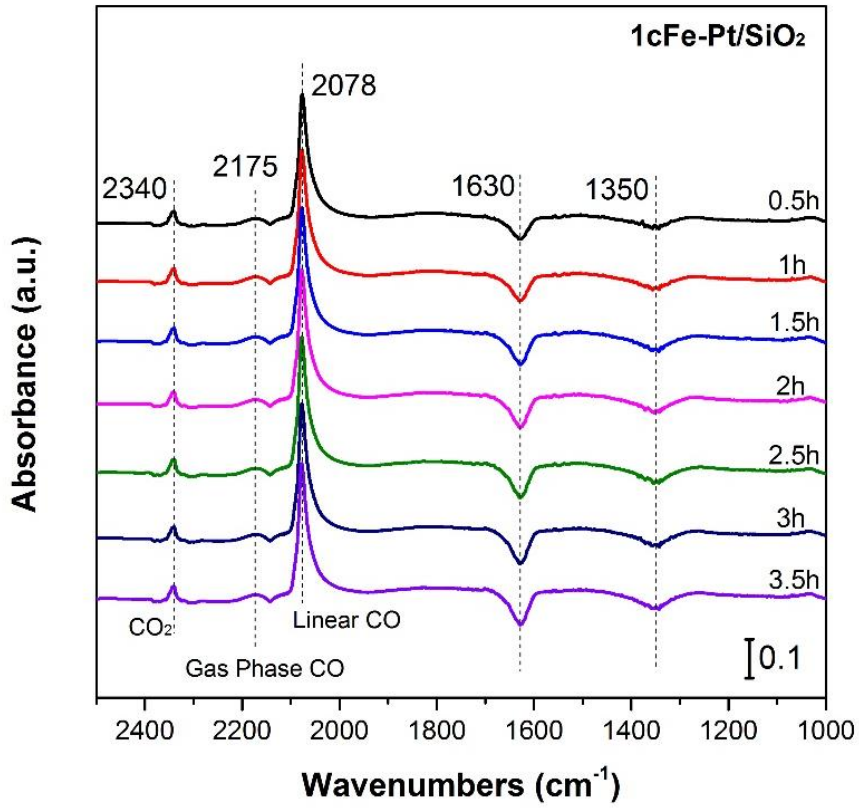

Supplementary Figure 18 | In situ DRIFTS measurements on the 1cFe-Pt/SiO_2 catalyst during the PROX reaction at room temperature. The DRIFT spectra were recorded after every 0.5 h. Reaction conditions: 1% CO, 0.5% O_2, and 48% H_2 balanced in helium at a flow rate of 30 ml/min; pressure = 0.1 MPa.

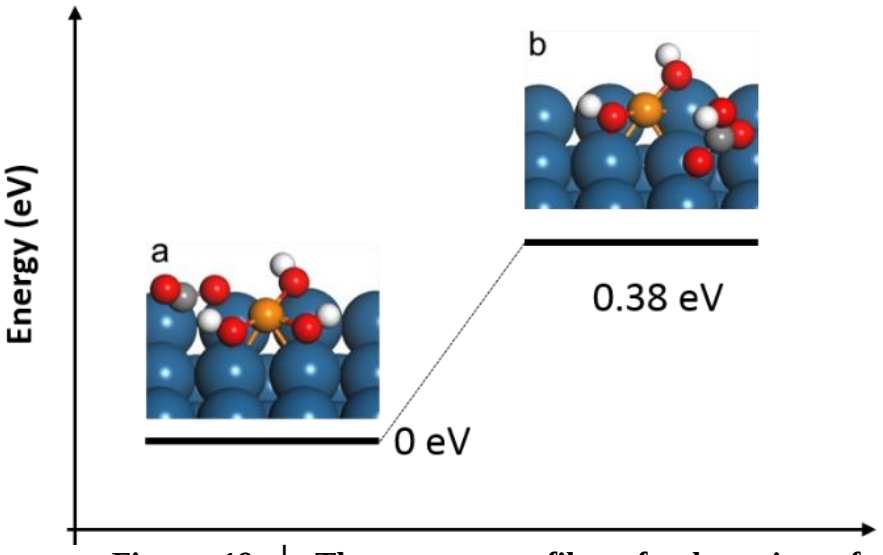

Supplementary Figure 19 | The energy profiles of adsorption of CO_2 on $Fe_1(OH)_3$@Pt(100) (a) and CO_3H on $Fe_1(OH)_2$@Pt(100) (b). Here Fe, O, H, and Pt atoms are in orange, red, white, and blue, respectively.

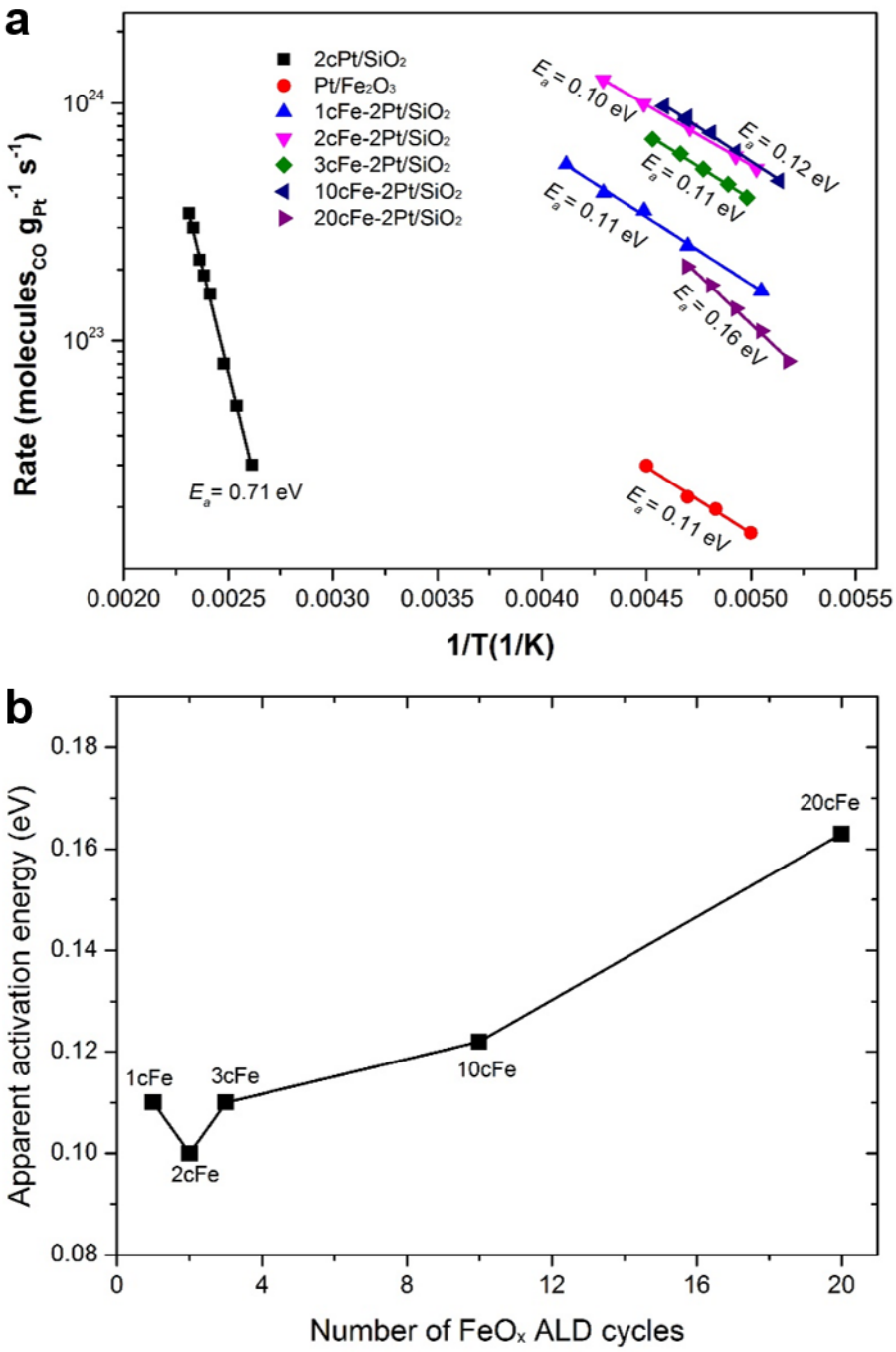

Supplementary Figure 20 | Catalytic performance of various Pt catalysts in the PROX reaction. a, reaction rates; **b**, the trend of apparent activation energies of xcFe-Pt/SiO_2 samples as a function of ALD cycles.

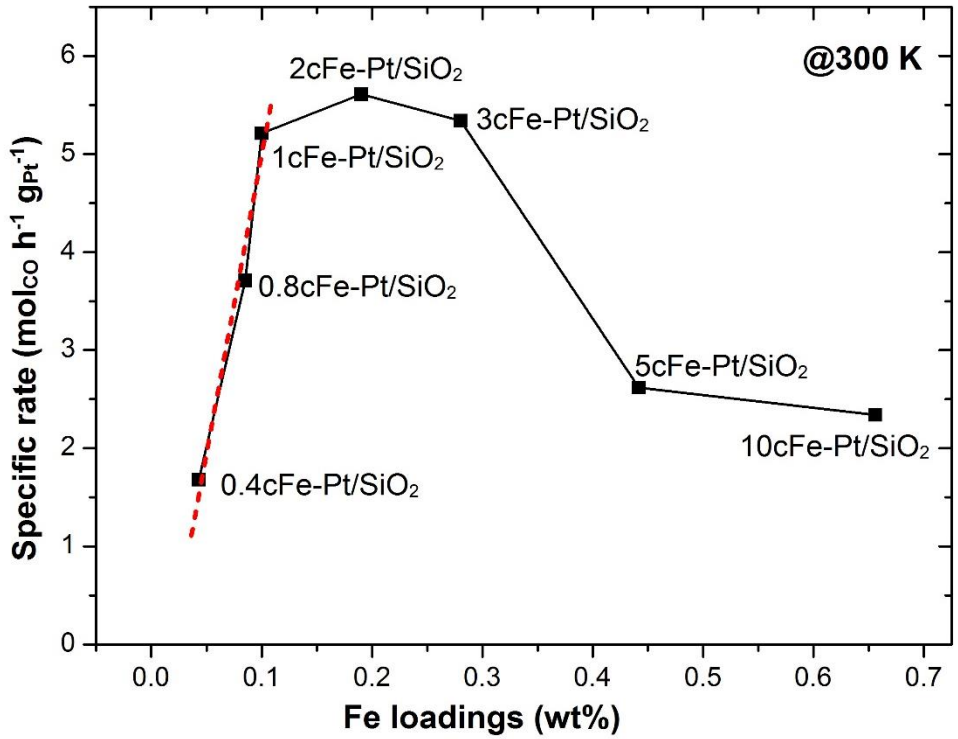

Supplementary Figure 21 | Mass specific rates as a function of Fe loadings over the *x*cFe-Pt/SiO_2 catalysts at 300 K. Here *x* = 0.4, 0.8, 1, 2, 3, 5, and 10 cycles. The red dash line is for guiding eyes. Note: the two samples of 0.4cFe-Pt/SiO_2, and 0.8cFe-Pt/SiO_2, were prepared using significant shorter $FeCp_2$ exposure time during FeO_x ALD. The Fe contents in these two samples are 0.043, and 0.085 wt%, respectively.

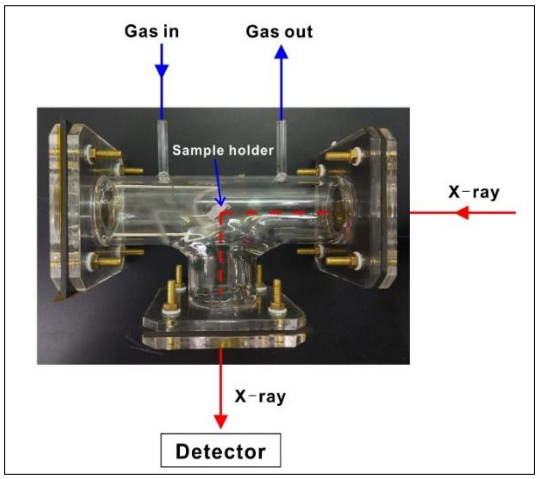

Supplementary Figure 22 | A photo of the XAFS quartz cell in a "T" shape, which allows recording XAFS spectra in both fluorescence and transmission mode.

The XAFS quartz cell

Considering the ultralow loading of Fe in our samples, any background Fe signals from the surroundings such as a stainless steel reactor would have a significant impact on our in situ measurements. Therefore, a quartz tube in a "T" shape was designed for the measurements (Supplementary Fig. 22). The windows were sealed by using Kapton foils along with O-rings and copper screws. The PROX or pretreatment gases were pre-mixed using mass flow controllers before reaching the XAFS cell. The sample is located in the middle reactor, and the sample temperature was calibrated before the XAFS measurements.

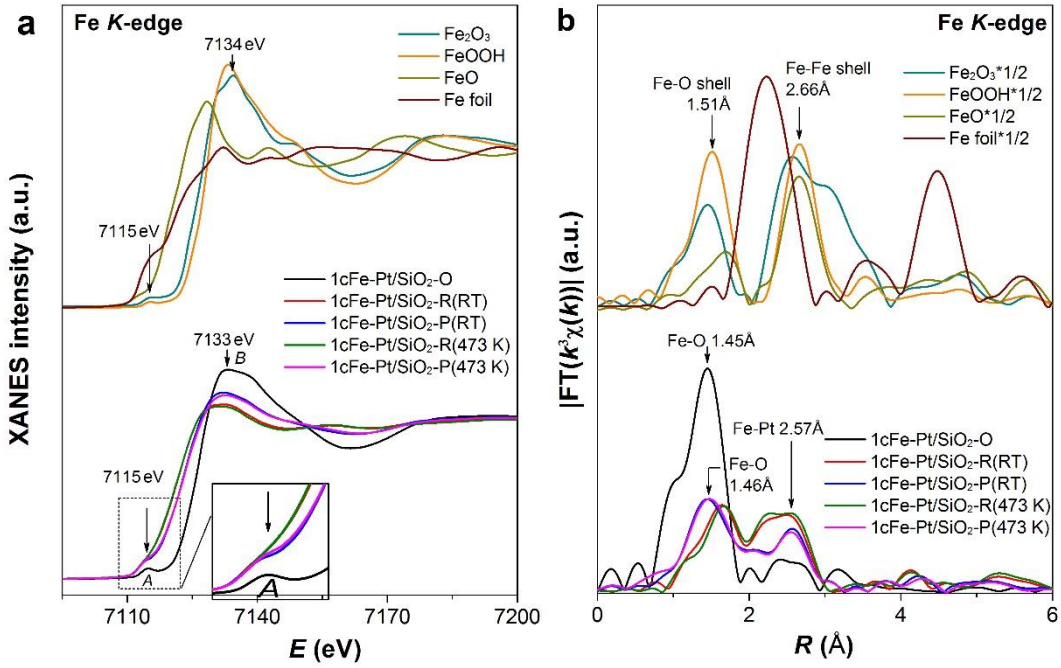

Supplementary Figure 23 | In situ XAFS measurements of the 1cFe-Pt/SiO_2 catalyst at the Fe K-edge under the conditions of as-prepared (1cFe-Pt/SiO_2-O), reduction at RT (1cFe-Pt/SiO_2-R), reduction at 473 K (1cFe-Pt/SiO_2-R(473K), PROX reaction at RT (1cFe-Pt/SiO_2-P) and PROX reaction at 473 K (1cFe-Pt/SiO_2-P(473K)). a, XANES spectra. **b,** FT spectra in R-space. The Inset in **a** shows the magnified pre-edge peak "***A***" in the dashed line rectangle.

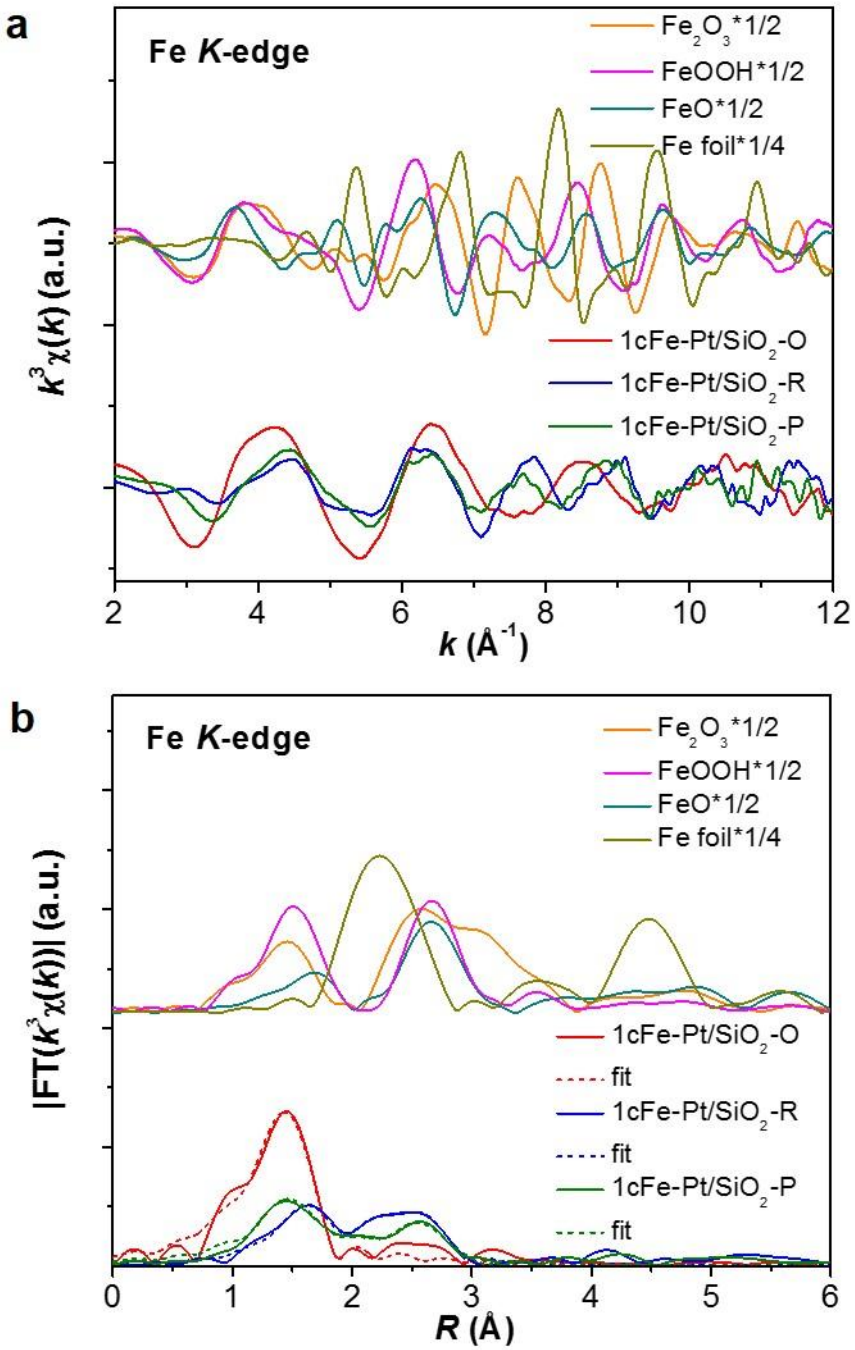

Supplementary Figure 24 | In situ XAFS data of the 1cFe-Pt/SiO_2 catalyst at the Fe K-edge. a, k^3-weighted EXAFS oscillations [$k^3\chi(k)$] for the 1cFe-Pt/SiO_2 catalyst at different conditions: as-prepared (1cFe-Pt/SiO_2-O), under 10% H_2 in helium at RT (1cFe-Pt/SiO_2-R), and under the RT PROX reaction (1cFe-Pt/SiO_2-P). **b,** the corresponding k^3-weighted Fourier transforms EXAFS spectra, as well as the fitting curves for 1cFe-Pt/SiO_2-O, 1cFe-Pt/SiO_2-R, and 1cFe-Pt/SiO_2-P. The EXAFS data of Fe foil, FeO, FeOOH and Fe_2O_3 compounds are shown as references

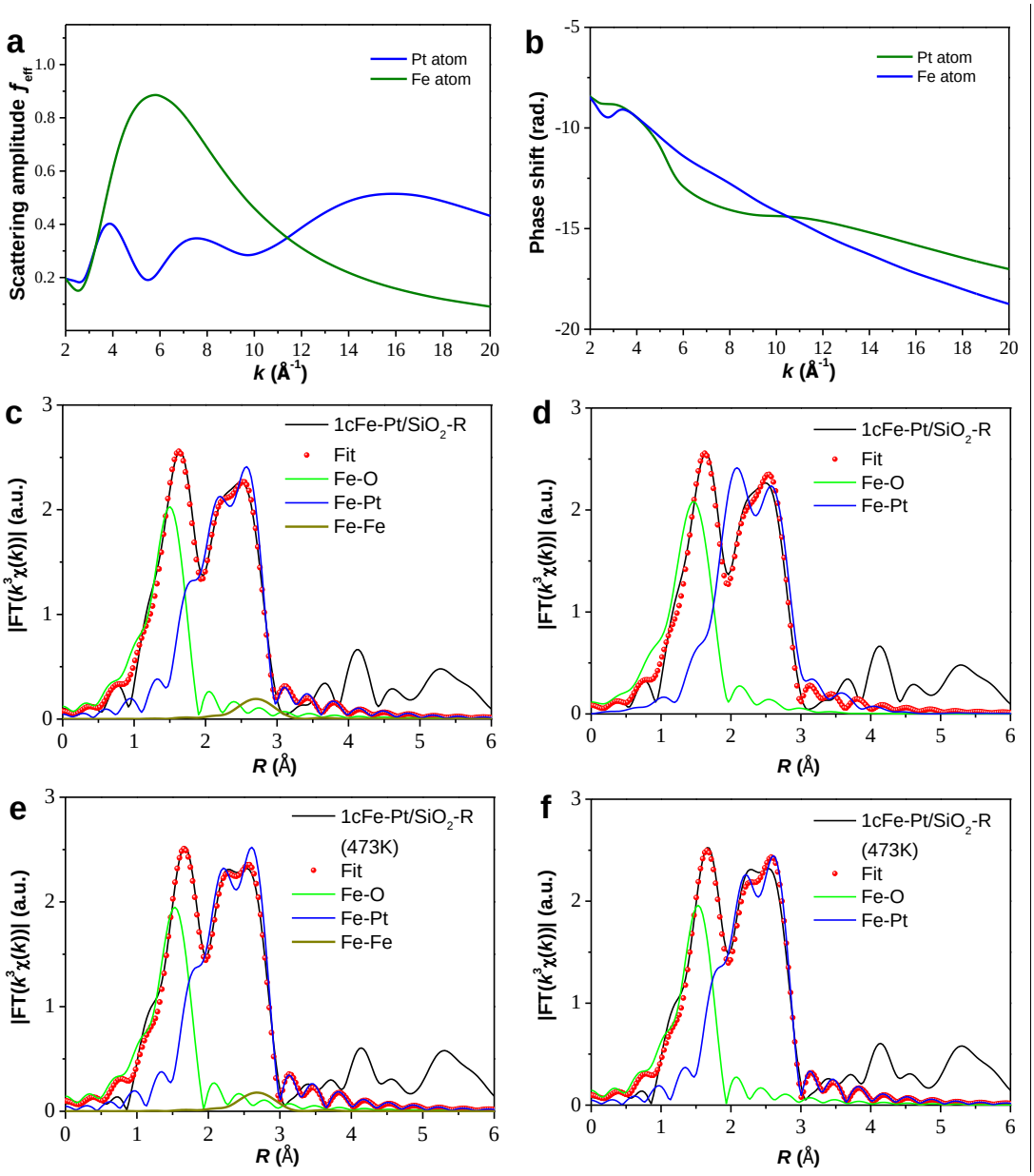

Supplementary Figure 25 | Comparisons of the Fe-Pt and Fe-Fe coordinations and the curve-fitting results of the 1cFe-Pt/SiO$_2$ sample using two structural models with and without the contribution of Fe-Fe coordination. Comparison of scattering amplitudes (**a**), and phase-shifts (**b**) between Fe and Pt atoms, which show significant differences in both cases. The curve-fitting results with (**c**) and without (**d**) the contribution of Fe-Fe coordination for the 1cFe-Pt/SiO$_2$-R sample. The curve-fitting results with (**e**) and without (**f**) the contribution of Fe-Fe coordination for the 1cFe-Pt/SiO$_2$-R(473K) sample.

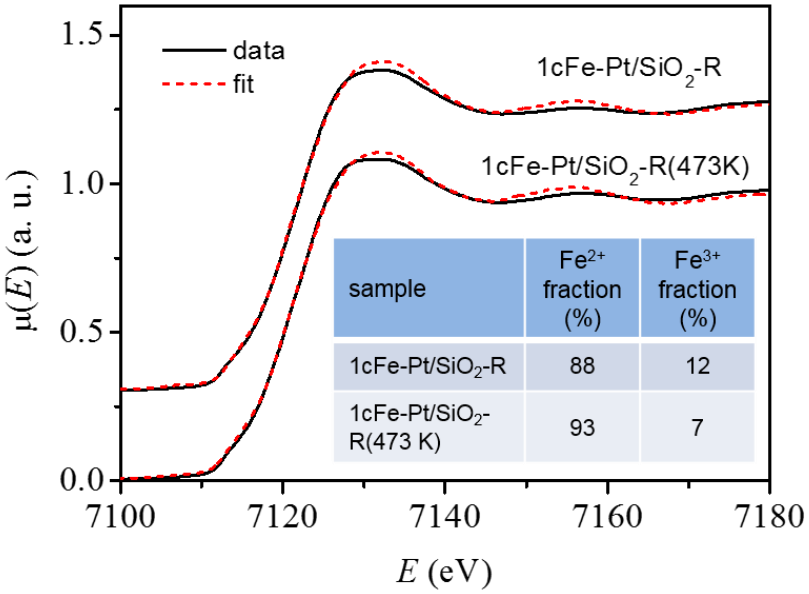

sample	Fe^{2+} fraction (%)	Fe^{3+} fraction (%)
1cFe-Pt/SiO_2-R	88	12
1cFe-Pt/SiO_2-R(473 K)	93	7

Supplementary Figure 26 | Linear combination analysis of the XANES spectra of the 1cFe-Pt/SiO_2 sample reduced at RT and 473 K. The XANES spectra of 0.4cFe-Pt/SiO_2-R(473K) and 0.4cFe-Pt/SiO_2-O were used as the standards for Fe^{2+} and Fe^{3+}, respectively. The inset shows the fractions of Fe^{2+} and Fe^{3+} oxide species in 1cFe-Pt/SiO_2-R and 1cFe-Pt/SiO_2-R(473K), respectively.

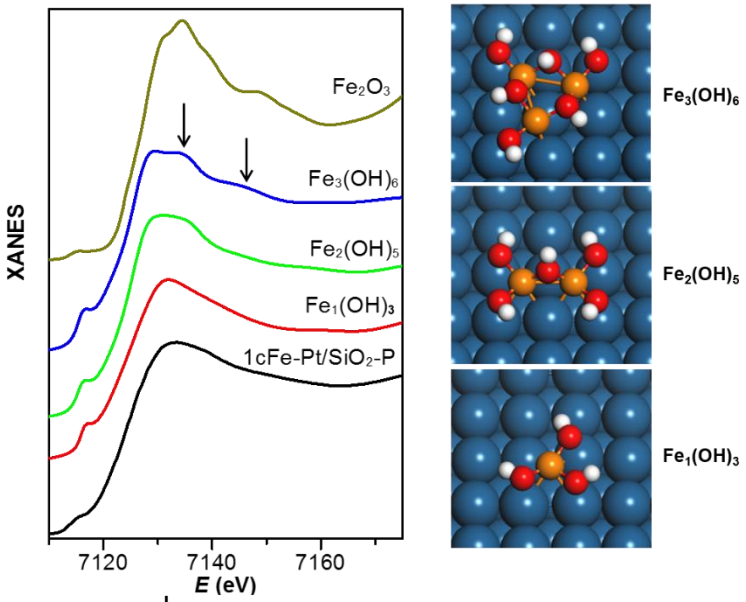

Supplementary Figure 27 | Comparison of the calculated XANES spectra. DFT optimized $Fe_1(OH)_3$ monomer, $Fe_2(OH)_5$ dimer and $Fe_3(OH)_6$ trimer were employed to simulate the XANES spectra and compare with the experimental spectra of 1cFe-Pt/SiO_2-P sample and Fe_2O_3 bulk.

<u>Quantitative XANES analysis</u>.

In order to further support the EXAFS results, we performed quantitative XANES linear combination analysis of 1cFe-Pt/SiO_2, by taking the spectrum of 0.4cFe-Pt/SiO_2-R(473K) as the standard for Fe^{2+} and the spectrum of 0.4cFe-Pt/SiO_2-O as the standard

for Fe^{3+}.

Please note that there are no such standard spectra of Fe^{2+} and Fe^{3+} available that can depict the Fe^{2+} and Fe^{3+} species in our samples. The spectra of FeO and Fe_2O_3 or $Fe(OH)_3$ could not be chosen as the standard for Fe^{2+} and Fe^{3+} species due to the large structure difference with our sample, which would give much worse fittings. The 0.4cFe-Pt/SiO_2 sample contains considerable lower Fe content of 0.043 wt%, its XANES spectra at oxidizing and reducing (473 K) condition could be the proper standard Fe^{2+} and Fe^{3+} spectra at the present stage.

As shown in Supplementary Fig. 24**,** the fraction of Fe^{3+} in 1cFe-Pt/SiO_2-R and 1cFe-Pt/SiO_2-R(473K) is very close to each other, consistent with our previous conclusion that increasing the sample temperature to 473 K would not cause any additional change at the Fe K-edge for 1cFe-Pt/SiO_2 (Supplementary Fig. 21). On the other hand, the fraction of Fe^{2+} in the reduced 1cFe-Pt/SiO_2 samples from quantitative XANES analysis is in the same trend as that of quantitative EXAFS fittings, where ~90% of iron species were atomically dispersed and ~10% of iron species were in the cluster form, this is because that iron (hydro)oxide clusters often require a significantly higher reduction temperature above 473 K[17,18].

We further compared the XANES spectra simulations for the $Fe(OH)_3$ monomer, $Fe_2(OH)_5$ dimer and $Fe_3(OH)_6$ trimer (Supplementary Fig. 25). The structures of the dimer and trimer were constructed and optimized by DFT calculations based on the monomeric $Fe_1(OH)_3$ structure, which will be discussed in the followings. Clearly, the calculated spectrum of $Fe(OH)_3$ monomer could well reproduce the overall spectral features of the experimental spetrum of 1cFe-Pt/SiO_2-P. With increasing the aggregation degree of $Fe(OH)_3$, i.e., from monomer, dimer to trimer, the calculated XANES spectrum gradually deviates from the experimental spetrum of 1cFe-Pt/SiO_2-P, and more peaks (labelled by arrows) emerge and their intensities are progressively increased. Comparing these peaks with the spectrum of Fe_2O_3 bulk suggests that these peaks are related to the Fe-Fe scattering and could be regarded as a fingerprint of aggregated $Fe_n(OH)_x$. Therefore, the absence of such peaks in the spectrum of 1cFe-Pt/SiO_2-P again confirms that the majority of the irons was in the isolated $Fe(OH)_3$ monomer, although other $Fe_n(OH)_x$ clusters (dimer, trimer, or multimers) might also exist in a minor fraction.

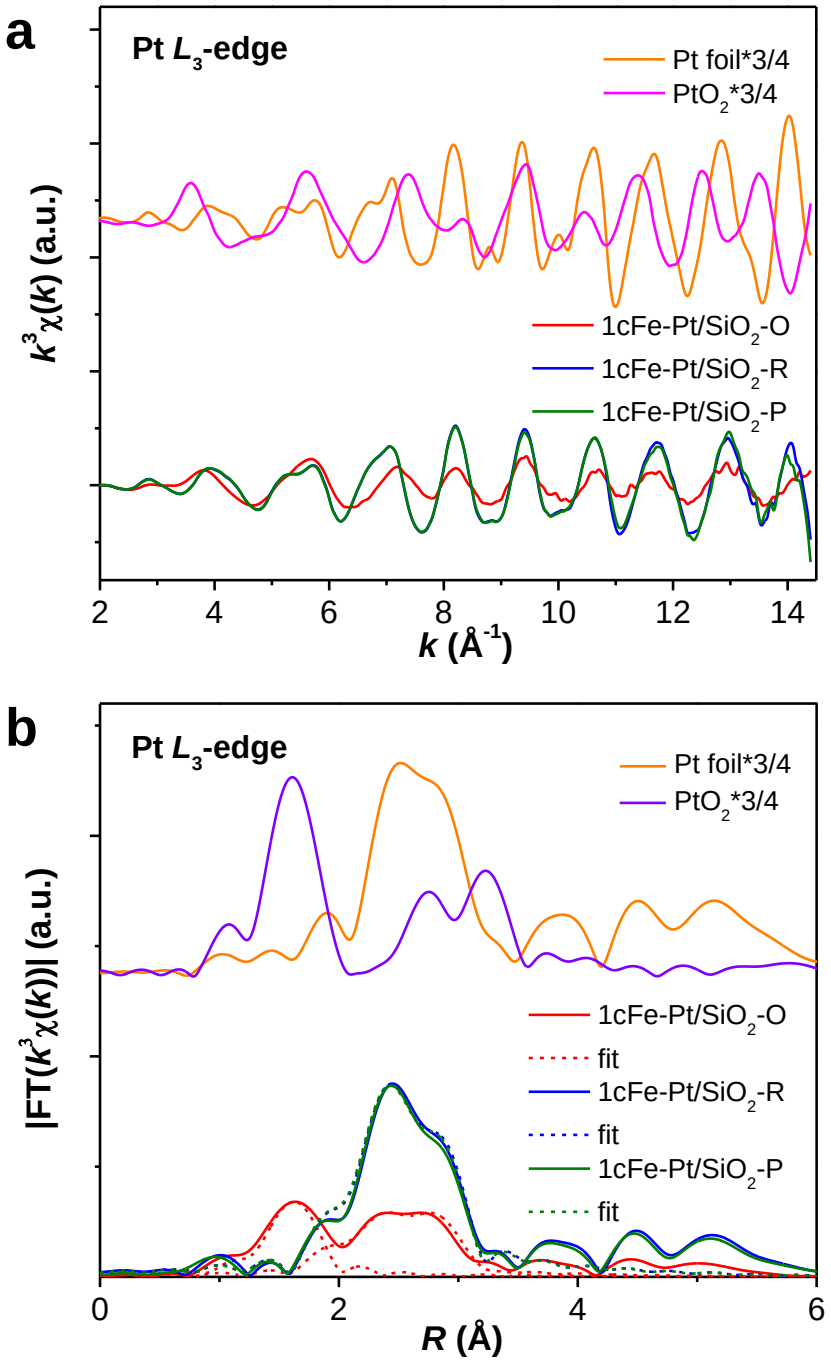

Supplementary Figure 28 | In situ XAFS data of the 1cFe-Pt/SiO_2 catalyst at the Pt L_3-edge. a, k^3-weighted EXAFS oscillations [$k^3\chi(k)$] for the 1cFe-Pt/SiO_2 catalyst at different conditions: as-prepared (1cFe-Pt/SiO_2-O), under 10% H_2 in helium at RT (1cFe-Pt/SiO_2-R), and under the RT PROX reaction (1cFe-Pt/SiO_2-P). **b,** the corresponding k^3-weighted Fourier transforms EXAFS spectra, as well as the fitting curves for 1cFe-Pt/SiO_2-O, 1cFe-Pt/SiO_2-R, and 1cFe-Pt/SiO_2-P. The EXAFS data of Pt foil and PtO_2 are shown as references.

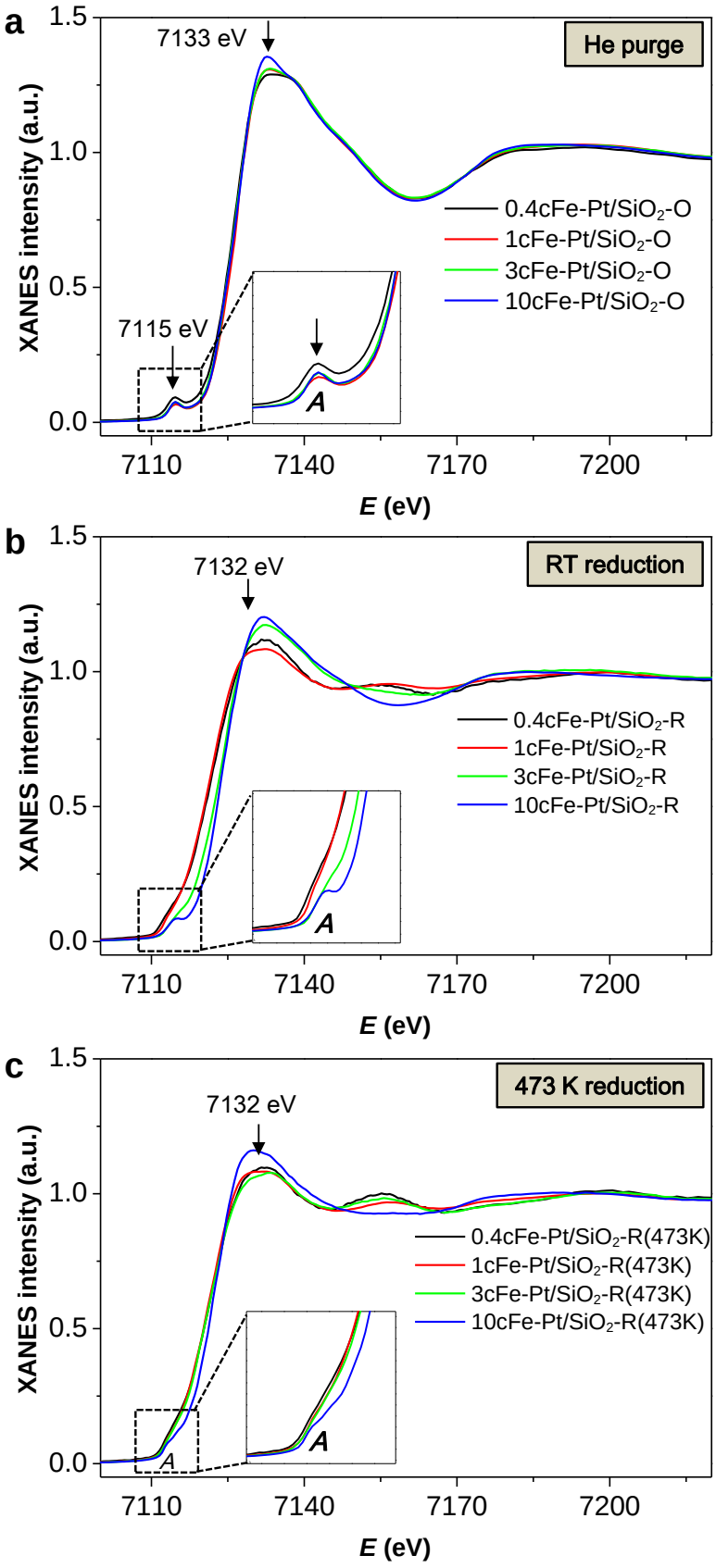

Supplementary Figure 29 | In situ XANES spectra of the *x*cFe-Pt/SiO$_2$ catalysts at the Fe K-edge under different conditions. a, He purge; **b**, RT reduction; **c**, 473K reduction. Here *x* = 0.4, 1, 3, and 10.

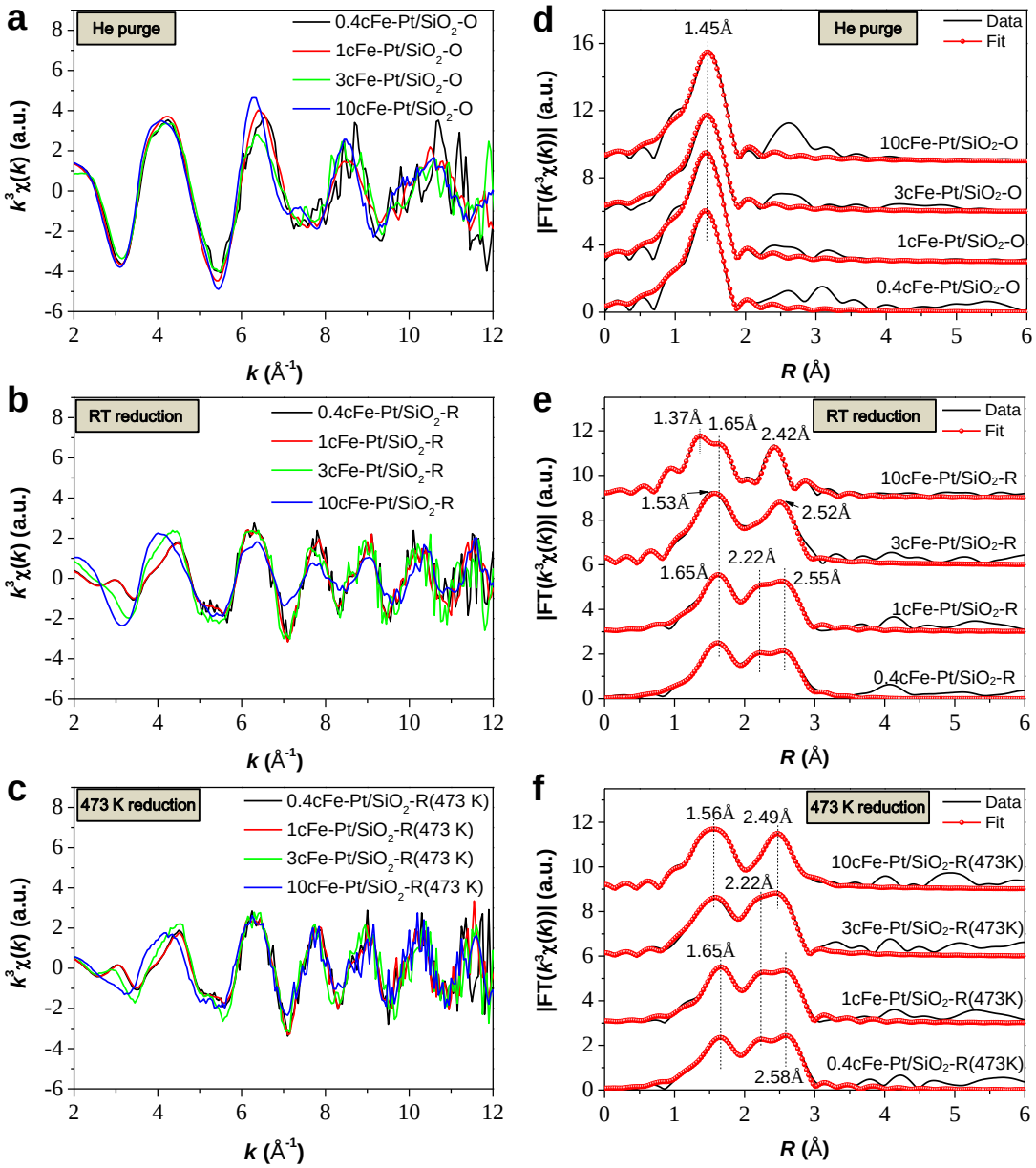

Supplementary Figure 30 | In situ EXAFS spectra of the *x*cFe-Pt/SiO$_2$ catalysts at the Fe K-edge. The EXAFS oscillation functions $k^3\chi(k)$ under the conditions of He purge (**a**), RT reduction (**b**) and 473 K reduction (**c**). The *R*-Space curve-fitting results under the conditions of He purge (**d**), RT reduction (**e**) and 473K reduction (**f**). Here *x* = 0.4, 1, 3, and 10.

Strategies of XAFS curve Fittings

The normalized XANES spectra for 0.4cFe-Pt/SiO$_2$, 1cFe-Pt/SiO$_2$, 3cFe-Pt/SiO$_2$, and 10cFe-Pt/SiO$_2$ under the conditions of He purge (denoted as *x*cFe-Pt/SiO$_2$-O), reduction at RT (denoted as *x*cFe-Pt/SiO$_2$-R) and reduction at 473 K (denoted as *x*cFe-Pt/SiO$_2$-R(473K)) are shown in Supplementary Fig. 29. The k^3-weighted EXAFS oscillation functions and the corresponding *R*-space curve-fitting results of these samples are shown in Supplementary Fig. 30.

For all the pristine samples (He purge, Supplementary Fig. 30d), only a strong Fe-O peak at 1.45 Å is observed. So, the fittings were performed by including a single Fe-O shell, within the *R*-range of 1.0-2.0 Å.

For the 0.4cFe-Pt/SiO_2 and 1cFe-Pt/SiO_2 samples reduced at RT and 473 K, the FT curves show a distinct peak at 1.65 Å assigned to the Fe-O coordination and a doublet peak at 2.22 and 2.55-2.58 Å assigned to the Fe-Pt and/or Fe-Fe coordinations (Supplementary Fig. 30e, f). Therefore, a three-shell structure model including a Fe-O, a Fe-Pt and a Fe-Fe shell was used to fit the EXAFS data of these two samples.

For the 10cFe-Pt/SiO_2-R sample, the FT curve shows an obvious splitting of the Fe-O peak where two peaks at 1.37 and 1.65 Å could be readily observed (Supplementary Fig. 30e). Comparing to the corresponding pristine samples (He purge, Supplementary Fig. 30d), it suggests that the new peak at 1.37 Å is originated from the unreduced Fe^{3+} oxide species, besides Fe^{2+}. For the 10cFe-Pt/SiO_2-R(473K) and the 3cFe-Pt/SiO_2 samples reduced at RT and 473 K (Supplementary Fig. 30e and f), the Fe-O peak positions are considerably shifted to the lower-R side of 1.53 and 1.56 Å, respectively, comparing to that (1.65 Å) for the reduced 0.4cFe-Pt/SiO_2 and 1cFe-Pt/SiO_2 samples. Such shifts are caused by the coexistence of Fe^{3+} species in the reduced 3cFe-Pt/SiO_2 and 10cFe-Pt/SiO_2 samples, as suggested by the persistence of the pre-edge peak "***A***" in the XANES spectra (Supplementary Fig. 29b, c). Therefore, another Fe-O shell has to be included to fit the data of the reduced 3cFe-Pt/SiO_2 and 10cFe-Pt/SiO_2 samples. Meanwhile, an additional Fe-Fe coordination should be also considered to account for the coexisting Fe^{3+} species when fitting the second peak at in the R-range of 2.42-2.52 Å for these samples. It should be noted that the number of shell was reduced from 4 to 3 for the second peak, compared to the previous fittings.

All the curve-fittings were performed using the ARTEMIS module implemented in the IFEFFIT package. Fittings were done in the *R*-space within the *R*-range of [1.0, 3.4] Å for k^3–weighted $\chi(k)$ functions with Hanning windows (dk = 1.0 $Å^{-1}$). For the reduced 0.4cFe-Pt/SiO_2 and 1cFe-Pt/SiO_2 samples, a *k*-range of 2.5–11.5 $Å^{-1}$ was used. The number of independent points for these two samples are $N_{ipt} = 2\Delta k \cdot \Delta R/\pi = 2 \times (11.5 - 2.5) \times (3.4 - 1.0)/\pi = 13$. For the reduced 3cFe-Pt/SiO_2 and 10cFe-Pt/SiO_2 samples, a *k*-range of 2.5–12.3 $Å^{-1}$ was used due to the better signal-to-noise ratios of the data, and the number of independent points $N_{ipt} = 2\Delta k \cdot \Delta R/\pi = 2 \times (12.3 - 2.5) \times (3.4 - 1.0)/\pi = 14$.

During curve fittings, the amplitude reduction factor S_0^2 was fixed at the value of 0.75 determined by fitting the data of Fe foil. For the Fe-O and Fe-Pt shells, each of the Debye–Waller factors (σ^2), coordination numbers (N) and interatomic distances (R), energy shift (ΔE_0) were treated as adjustable parameters. For the Fe-Fe coordination, N and R were treated as adjustable parameters, while the σ^2 and ΔE_0 were set as those for Fe-Pt coordinations to reduce the number of adjustable parameters. For the reduced 3cFe-Pt/SiO_2 and 10cFe-Pt/SiO_2 samples, a second Fe-O shell and a second Fe-Fe shell are required as mentioned above. For the second Fe-O shell, its σ^2 and ΔE_0 were set equal to those for the first Fe-O shell while the N and R were treated as adjustable parameters. For the second Fe-Fe shell, its σ^2 was set equal to those for the first Fe-Fe shell, the N and R were treated as free parameters, while the ΔE_0's for the two Fe-Fe coordinations was set at the best-fit value (-6.2 eV) for the 1cFe-Pt/SiO_2-R sample. Setting the ΔE_0 for the Fe-Fe coordination has advantages of reducing the number of adjustable parameters and breaking the strong correlation between ΔE_0 and R. This should be reasonable, since during our fittings for the 0.4cFe-Pt/SiO_2 and 1cFe-Pt/SiO_2 samples, we found that the ΔE_0's for the Fe-Fe coordinations were changed in a narrow

range, i.e., from -4.9 to -7.5 eV (Supplementary Table 6). We also checked that within the range of [-4.9, -7.5] eV, the different choice of ΔE_0's for the Fe-Fe coordinations of the reduced 3cFe-Pt/SiO_2 and 10cFe-Pt/SiO_2 samples actually did not influence the results considerably. The number of adjustable parameters for the reduced 0.4cFe-Pt/SiO_2 and 1cFe-Pt/SiO_2 samples is $N_{para} = 4 + 4 + 2 = 10$, less than $N_{ipt} = 13$; for the 3cFe-Pt/SiO_2 and 10cFe-Pt/SiO_2 samples reduced at both RT and 473 K, $N_{para} = 4 + 2 + 3 + 2 + 2 = 13 < N_{ipt} = 14$.

Following these strategies, the curve-fitting results are shown in Supplementary Fig. 30 and the parameters are listed in Supplementary Table 6. All the yielded *R*-factors are not larger than 0.008, indicating the good fitting qualities.

Quantification of iron hydroxide clusters in the *x*cFe-Pt/SiO_2 catalyst

Based on our comprehensive fittings, we found that the curve-fitting results using the structural models with and without the contribution of Fe-Fe coordination do not show a big difference for the 1cFe-Pt/SiO_2 sample reduced at both RT and 473 K (Supplementary Fig. 25). While the structural model with the Fe-Fe scatter gives a slightly better curve-fitting (Supplementary Fig. 25c and e). The fitting result showed a low Fe-Fe coordination of $N_{Fe\text{-}Fe} = 0.3$ (Supplementary Table 6). Therefore, the contribution from the Fe-Fe scatter could be small, and we could safely conclude that a dominant majority (~90%) of Fe atoms are in the form of isolated Fe species in the 1cFe-Pt/SiO_2 sample.

The fraction of isolated Fe species in the sample was calculated according to the equation:

$$X_{Fe1} = [1 - (N_{Fe\text{-}Fe}/N_{iron\text{-}hydroxide\text{-}cluster})] \times 100\% \quad (1)$$

X_{Fe1} is the fraction of isolated Fe_1 species; $N_{iron\text{-}hydroxide\text{-}cluster}$ is the Fe-Fe CNs in iron hydroxide clusters, which might vary from 1-6 for different cluster sizes. Here we took 3 as the average of Fe-Fe CNs for the tiny iron hydroxide clusters on Pt nanoparticles[19]. The fraction of isolated Fe_1 species in our sample could be determined to be $X_{Fe1} \approx [1-(0.3/3)] \times 100\% = 90\%$.

Certainly,

If we take 1 as the Fe-Fe CNs for the iron dimers, $X_{Fe1} \approx [1- (0.3/1)] \times 100\% = 70\%$.

If we take 2 as the Fe-Fe CNs for the iron trimers, $X_{Fe1} \approx [1- (0.3/2)] \times 100\% = 85\%$.

If we take 6 as the Fe-Fe CNs for the FeOOH bulk, $X_{Fe1} \approx [1- (0.3/6)] \times 100\% = 95\%$.

Therefore, it could still safely conclude that the majority (70%-95%) of the irons were in the isolated $Fe(OH)_3$ form. This fraction is in an excellent agreement with the STM result (82%) which will be discussed in the following.

As increasing Fe loadings, the fraction of isolated Fe sites decreases and iron hydroxide clusters becomes more and more considerable, manifested by the substantial increase of the Fe-Fe CNs (Supplementary Table 6), which were about 1.0 and 2.5, for the 3cFe--Pt/SiO_2-R, and 10cFe-Pt/SiO_2-R catalysts, respectively. Apparently, the amount of iron hydroxide clusters was considerable in 3cFe-Pt/SiO_2-R (~30%) and became dominant (>80%) in the 10cFe-Pt/SiO_2 sample according to the equation (1).

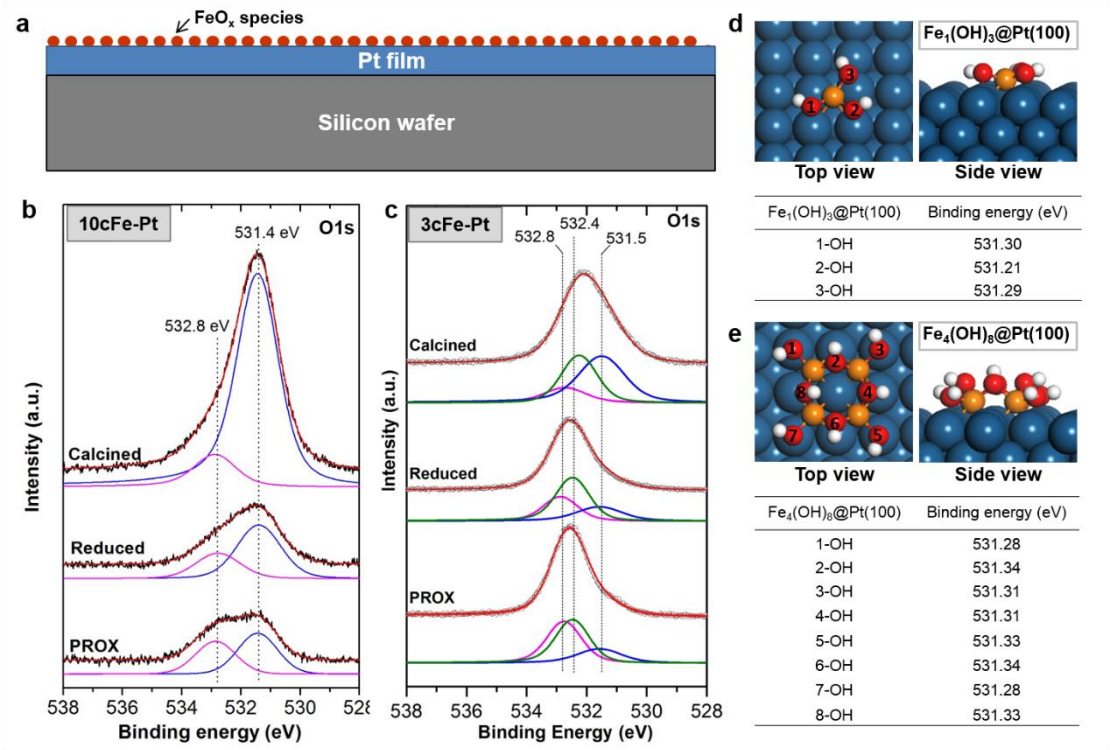

Supplementary Figure 31 | XPS studies of the *x*cFe-Pt film model catalyst and DFT calculations on the OH binding energies in $Fe_1(OH)_3$ and $Fe_4(OH)_8$ clusters supported on Pt(100). a, schematic illustration of the *x*cFe-Pt film model catalyst. XPS O 1s spectra of the 10cFe-Pt (**b**) 3cFe-Pt (**c**) film model catalysts after calcining in 10% O_2 in Ar at 473 K for 30 min, reducing in 10% H_2 in argon at 473 K for 30 min, and treatment with the PROX reaction gas at room temperature for 60 min, respectively. In this case, the PROX reaction gas consists of 1% CO, 0.5% O_2, and 5% H_2 balanced in Argon. **d**, the top and side views of $Fe_1(OH)_3$@Pt(100) as well as the calculated OH binding energies. **e**, the top and side views of $Fe_4(OH)_8$@Pt(100) as well as the calculated OH binding energies.

XPS studies of the 3cFe-Pt and 10cFe-Pt film model catalyst.

After calcining the 10cFe-Pt film model catalyst in 10% O_2 in Argon at 473 K for 30 min, we observed that the O1s peak was dominantly located at ~531.4 eV with a shoulder at 532.8 eV which is assigned to hydroxyls and chemisorbed water species, overlapping with signal from minor amounts of oxygenated carbonaceous compounds, respectively (Supplementary Fig. 31b)[20,21]. Surprisingly, we did not observe any noticeable lattice oxygen species of FeO_x at a lower binding energy of 529.7 eV, which might be due to hydration, either by humid air during the sample shipping or by the trace amount of background water in the ambient pressure cell. Indeed, Bao *et al.* also reported the hydroxylation of FeO_2 film by trace water vapor in the high pressure gas after oxidation in 1 bar O_2[21].

Reducing the 10cFe-Pt film model catalyst at 10% H_2 in Argon at 473 K for 30 min significantly reduced the intensity of O1s peak at 531.4 eV, which might be due to reduction of Fe_nO_x. Exposing the sample to PROX reaction gas at room temperature did not significantly change the intensity of the O1s peak at 531.4 eV, but induced remarkable formation of water indicated by the growth of the peak at 532.8 eV. In brief,

the Fe_nO_x species grown by ALD seems to be fully hydroxylated during these steps.

On the 3cFe-Pt film sample, XPS showed a broad O1s peak which can be deconvoluted into three peaks located at 531.5, 532.4 and 532.8 eV (Supplementary Fig. 31c). Again, we did not observe any noticeable lattice oxygen species of FeO_x at a lower binding energy of 529.7 eV, consistent with the 10cFe-Pt film sample (Supplementary Fig. 31b). The peak at 532.8 eV is assigned to chemisorbed water combined with minor amounts of oxygenated carbonaceous compounds. However, on this sample, a Si 2p signal in the binding energy range of SiO_2 was also detected (not shown here). The signal is interpreted to come from the oxidized Si substrate underneath the Pt thin film. For the 10cFe-Pt film sample, no such Si 2p signal was detected through the Pt thin film. The deconvoluted peak at ~532.4 eV was therefore assigned to oxygen atoms in the SiO_2 substrate underneath the Pt thin film. The intensity contribution from SiO_2 to the 3cFe-Pt O1s was estimated from the Si 2p intensity after taking into account the relative photoelectric cross sections. The peak at 531.5 eV was assigned to the O species in $Fe_n(OH)_x$ in the 3cFe-Pt film sample.

According to the EXAFS quantification, there were about 70% atomically dispersed $Fe_1(OH)_3$ in the 3cFe-Pt/SiO_2 sample, while $Fe_n(OH)_x$ clusters became dominant in 10cFe-Pt/SiO_2 (Supplementary Figs. 29 and 30 and Supplementary Table 6). Therefore, Similar OH binding energies observed in 3cFe-Pt and 10cFe-Pt film model catalysts (Supplementary Fig. 31b,c) suggest that the OH binding energy of OH in atomically dispersed $Fe_1(OH)_3$ and $Fe_n(OH)_x$ clusters are similar.

To further verify the above XPS results, the OH binding energies for $Fe_1(OH)_3$ and $Fe_4(OH)_8$ supported on Pt(100) were calculated for comparison. It was found that the binding energies of OH in $Fe_1(OH)_3$ clusters are 531.2-531.3 eV (Supplementary Fig. 31d), identical to the ones in $Fe_4(OH)_8$ (Supplementary Fig. 31e). Therefore, Fe-Fe coordination appears to have negligible impact on the binding energy of OH in $Fe_n(OH)_x$ clusters, consistent very well with the XPS results (Supplementary Fig. 31b,c).

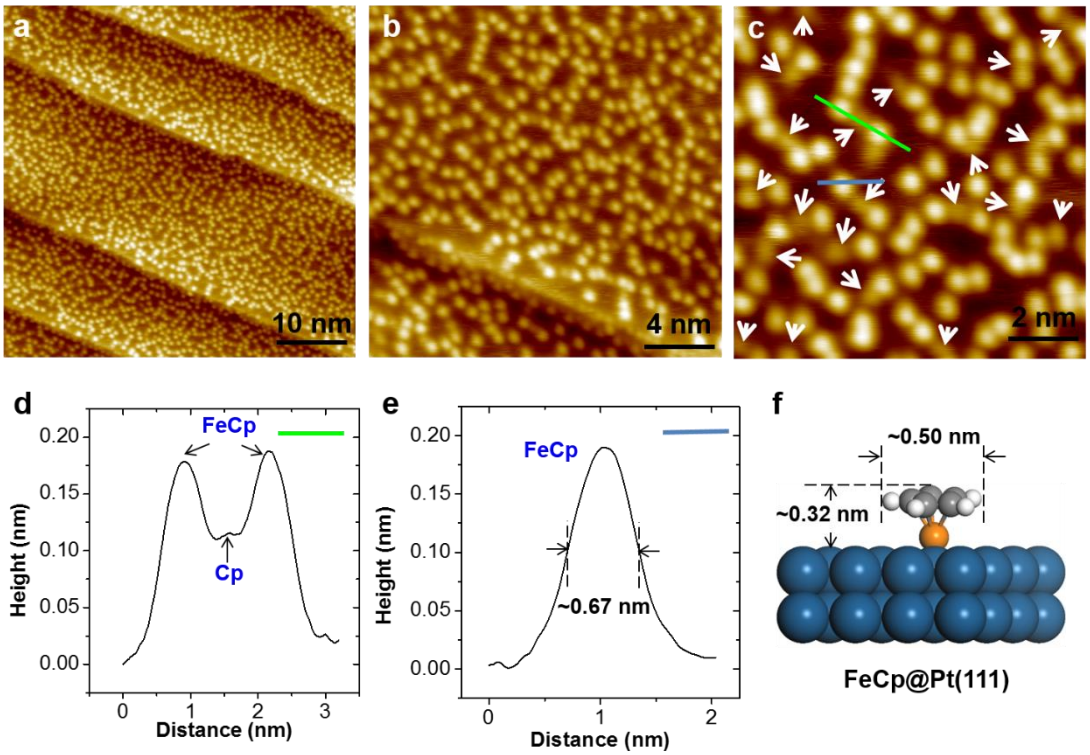

Supplementary Figure 32 | STM images of chemisorbed $FeCp_2$ on Pt(111) surface at different magnifications after exposing to ~100 L $FeCp_2$ at 393 K (a-c). The white arrows in (**c**) highlight the darker features, compared to the rest of much brighter ones. **d,** the height profile along the green line in (**c**). **e,** the height profile along the blue line in (**c**). **f**, The size information of optimized chemisorbed FeCp on Pt(111). The scanning parameters are V = -1.5 V, I = 100 pA; V = -1.5 V, I = 100 pA; and V = -1.5 V, I = 50 pA for (A-C), respectively.

Dissociative chemisorption of $FeCp_2$ on Pt(111)

STM was carried out to directly investigate the surface chemistry of FeO_x ALD on Pt(111) single crystal surface. The Pt crystal was exposed to ~100 L $FeCp_2$ at 393K, similar to the FeO_x ALD conditions. STM images in Supplementary Fig. 32a-c clearly showed that these features were uniformly dispersed on the Pt(111) surface. Two types of species with a height of ~0.2 nm and ~0.11 nm were identified as shown in Supplementary Fig. 32c-e. According to literature [22], these two types of features can be assigned to FeCp* and Cp* (the asterisk designates a surface species), respectively. The size of the chemisorbed FeCp* measured by STM (Supplementary Fig. 32e) is very close to one from the DFT calculated FeCp structure (Supplementary Fig. 32f). The Cp* species are highlighted by the white arrows in Supplementary Fig. 32c. Independently, Zemlyanov *et al.* also reported that ferrocene adsorbed dissociatively on Pt(111) surface mainly as Cp (cyclopentadienyl ring) at 300 K at low exposures[23].

In addition, dissociative chemisorption of metal organic precursors on metal surfaces during ALD processes was also found in other systems. Zaera, *et al.* investigated the surface chemistry for Cu ALD on Ni(110) using copper(I) *N,N'*-di-sec-butylacetamidinate [(Cu(^{s}Bu-amd))$_2$] and hydrogen [24,25]. They found that (Cu(^{s}Bu-amd))$_2$ dissociatively adsorbed on the nickel surface at above 300 K. Stair *et al.* also reported that trimethylphosphine-(hexafluoroacetylacetonato)silver(I) [(hfac)Ag-(PMe_3)] dissociatively chemisorbs on the Ag surface by forming Ag(hfac) surface

species while releasing the PMe_3 ligand during Ag ALD at 443K[26]. Moreover, we recently showed that dissociative chemsorption of trimethyalumium [$Al(CH_3)_3$] on noble metal surfaces such as Pd, Pt, and Ir is a general process by forming $AlCH_3$ and CH_3* surface species[27]. We also found that the bis(ethylcyclopentadienyl)ruthenium [$Ru(EtCp)_2$] undergoes dissociative chemisorption on the existing Ru metal surface to form Ru(EtCp)* and EtCp* surface species during the $Ru(EtCp)_2$ exposure at 423 K [28].

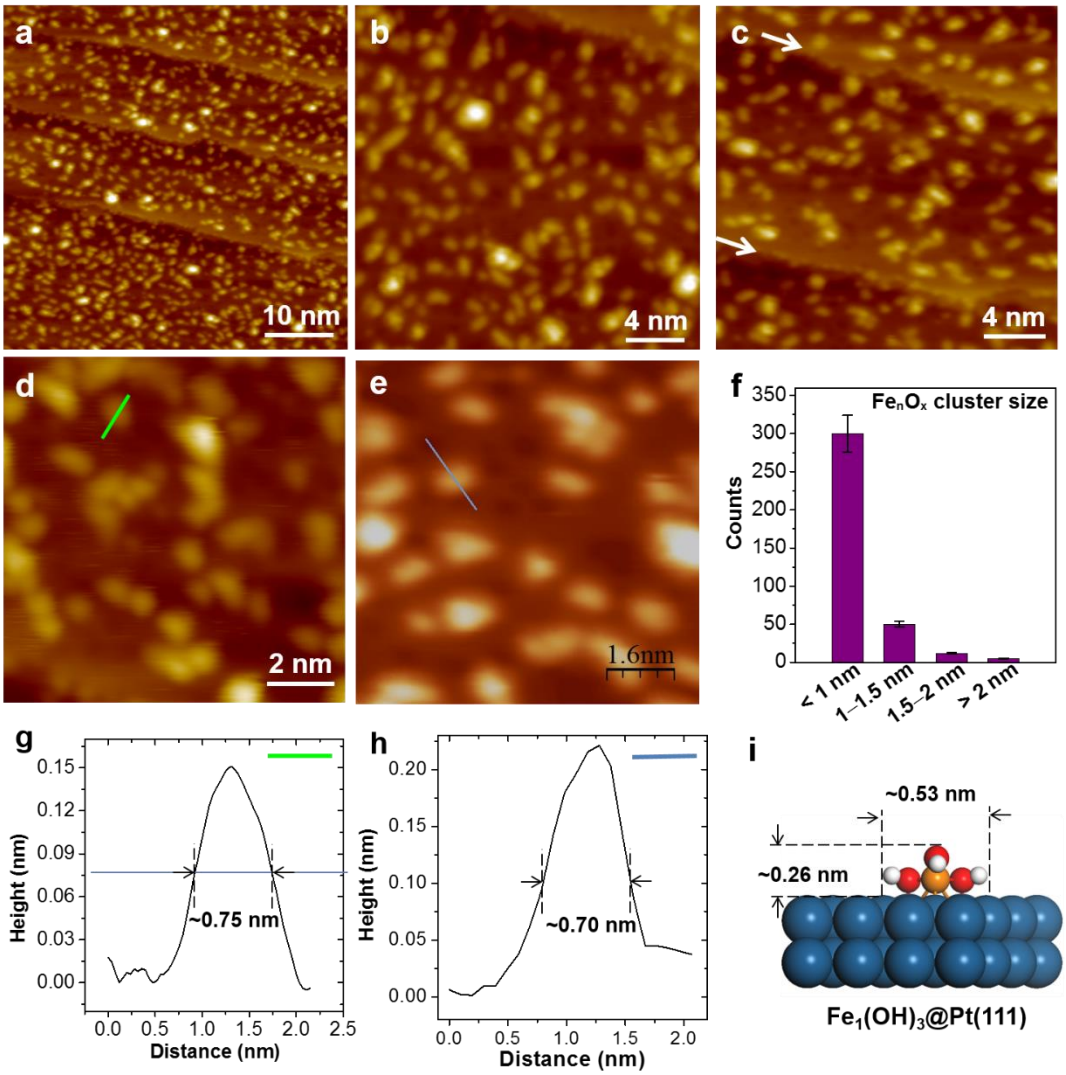

Supplementary Figure 33 | STM images of one cycle of FeO_x ALD on Pt(111) surface at different magnifications (a-e). Here one cycle FeO_x ALD was performed by oxidizing the chemisorbed $FeCp_2$ on Pt(111) in 1 $\times 10^{-6}$ mbar O_2 at 473 K for 30 min, followed by another annealing step by closing the O_2 source at 473 K for another 30 min. **f**, Fe_nO_x cluster size distribution (The error bars in **f** are determined by 8% of the counts). **g,** the height profile along the green line in (**d**); **h,** the height profile along the blue line in (**e**); **i**, the size information of optimized chemisorbed $Fe_1(OH)_3$ on Pt(111). The white arrows in (**c**) highlights the atomic steps of Pt(111) surface. The scanning parameters for (**a-d**) are all V = -1.5 V, I = 100 pA.

Formation of subnanometer Fe_nO_x clusters on Pt(111) by ALD

A large fraction of ultrafine Fe_nO_x species with subnanometer size in diameter and

about 0.15 nm in height were formed after performing one cycle of FeO_x ALD on the Pt(111) surface (Supplementary Fig. 33). This observation is in good agreement with the STM results reported by Zemlyanov et al where subnanometer Fe_nO_x clusters less than 1 nm size were dominant on the Pt(111) surface after one FeO_x deposition cycle, consisted of exposure of Pt(111) to 90 L ferrocene at 300 K followed by subsequent exposure to 1×10^{-6} mbar O_2 for 10 min at 625 K[23]. The size of these tiny Fe_nO_x species are comparable to the chemisorbed FeCp* species in Supplementary Fig.32. Therefore, these ultrafine Fe_nO_x clusters are likely isolated Fe_1O_x species.

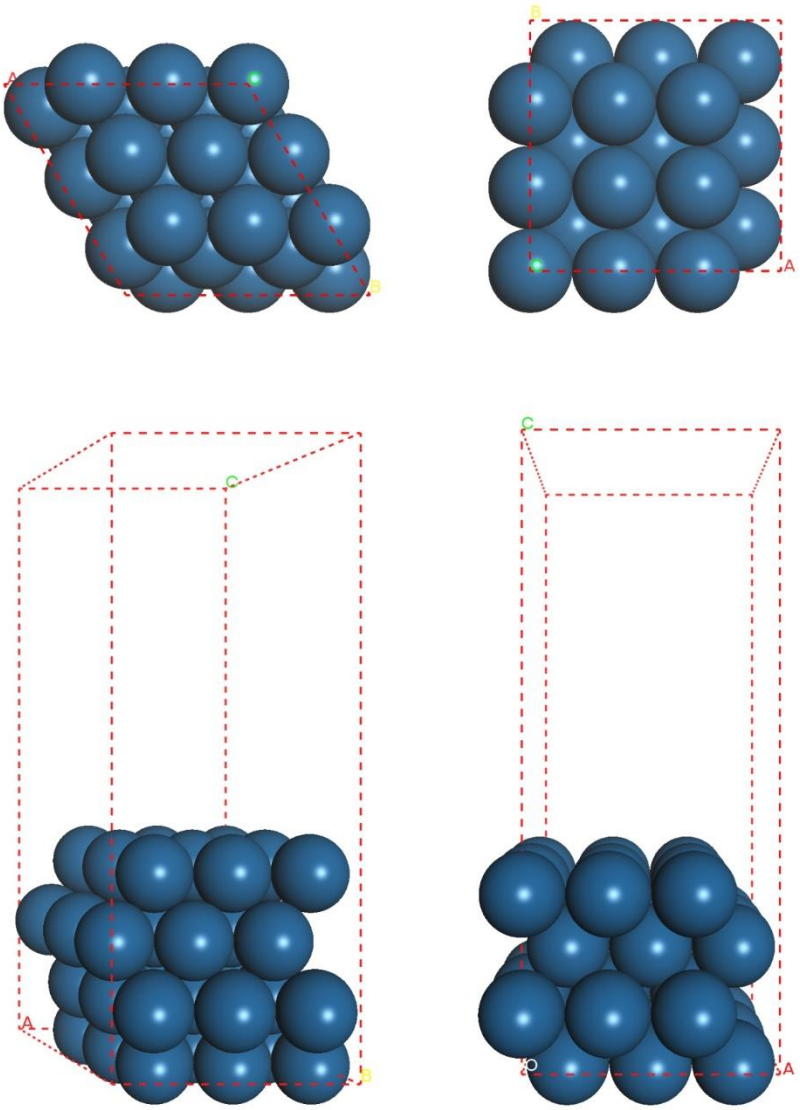

Supplementary Figure 34 | Top and side views of Pt(111) (left) and Pt(100) (right) slabs. Pt atoms in blue.The calculated crystal lattice parameter of Pt is 3.96 Å, and it is very close to experimental value of 3.91 Å. The Pt(100) and Pt(111) were modelled by four-layer periodic slab with (3 × 3) supercell; and top two layers were relaxed and fixed two bottom layers in its bulk distances. The vacuum slab was set up to 15 Å.

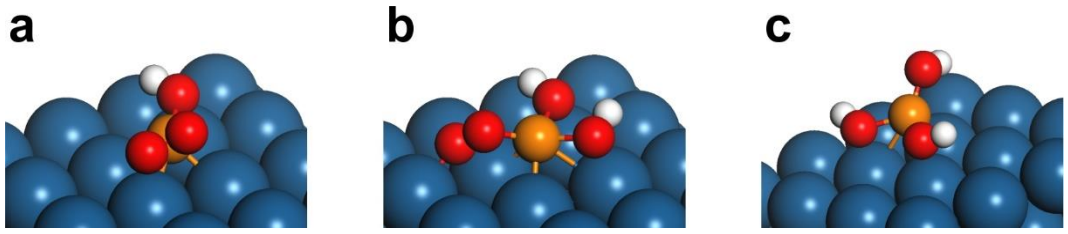

Supplementary Figure 35 | The potential catalyst candidates according to our calculations. a, $Fe_1(OH)O_2$ supported on Pt(100): $Fe_1(OH)O_2$@Pt(100). **b,** $Fe_1(OH)_2O_2$ supported on Pt(100): $Fe_1(OH)_2O_2$@Pt(100). **c,** $Fe_1(OH)_3$ supported on Pt(111): $Fe_1(OH)_3$@Pt(111). Here H atoms are in white, O atoms are in red, Fe atoms are in orange, and Pt atoms are in blue.

Potential catalyst candidates:

$Fe_1(OH)O_2$@Pt(100) (Supplementary Fig. 35a) and $Fe_1(OH)_2O_2$@Pt(100) (Supplementary Fig. 35b) might be other possible structures showing similar coordination numbers and length of the Fe-O and Fe-Pt bonds. However, the calculated binding energy of the O atom binding to Pt in both cases is about 530.4 eV, significantly lower than our experimental result (Supplementary Fig. 31).

We also evaluated the adsorption of $Fe_1(OH)_3$ on Pt(111), named as $Fe_1(OH)_3$@Pt(111), and found that one of the OH groups binding to the Fe atom atop, slantly to the Pt(111) surface is the most stable configuration (Supplementary Fig. 35c). In this case, the calculated bond lengths of Fe-OH are 1.95, 1.95 and 1.80 Å and Fe-Pt distances are 2.51, 2.95, and 2.98 Å (Supplementary Table 8), which differ significantly from the EXAFS results in Supplementary Table 6. It is worth noting that the adsorption energy of Fe atom on Pt(111) and Pt(100) is -5.02 and -5.75 eV, respectively, indicating anchoring Fe on Pt(100) is more favorable than on Pt(111). Therefore, the above experimental results and theoretical calculations both suggest that $Fe_1(OH)_3$@Pt(100) is the dominant species during the PROX process.

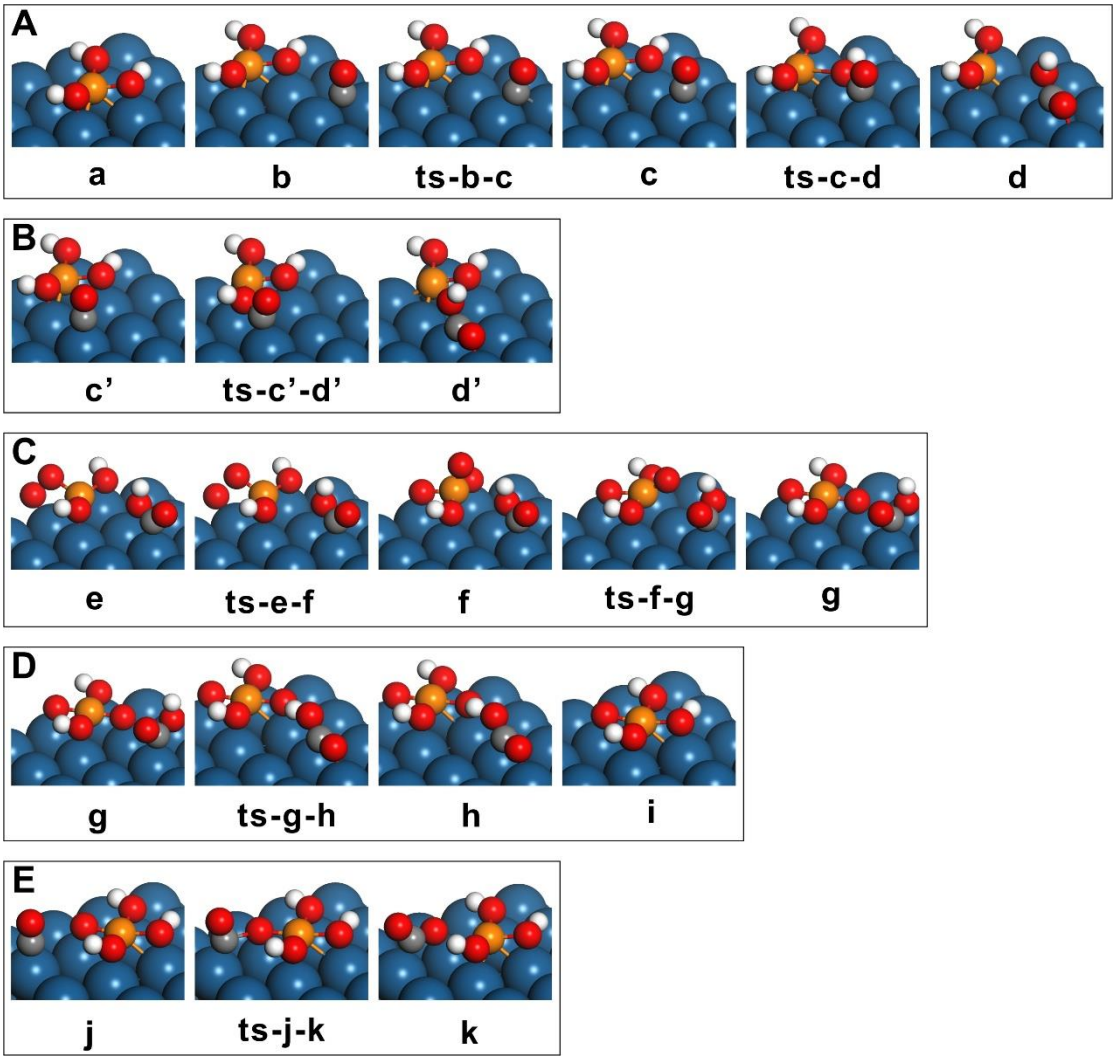

Supplementary Figure 36 | The detailed reaction steps involved in the CO oxidation on $Fe_1(OH)_3$@Pt(100). **(A)** CO chemisorption and association with the elongated OH group to form COOH species: **a**, the initial state of $Fe_1(OH)_3$@Pt(100); **b**, CO chemisorption at the bridge sites of Pt surface; **c**, CO transformation to the Pt atop sites; **d,** COOH formation by associating with the elongated OH group and forming $Fe_1(OH)_2$@Pt(100). **(B)** The alternative reaction pathway to form COOH on $Fe_1(OH)_3$@Pt(100) by reacting with the OH group with a short bond length: **c',** linear CO at the Pt atop sites; **d'**, COOH formation on $Fe_1(OH)_3$@Pt(100) by reacting with the OH group with a short bond length. **(C)** O_2 activation on $Fe_1(OH)_2$@Pt(100) configuration: **e,** O_2 adsorption on $Fe_1(OH)_2$@Pt(100) configuration; **f,** O_2 activation via one O flipping onto the Fe atop site of $Fe_1(OH)_2$@Pt(100); **g**, the O at the Fe atop sites flipped over to the bridge site between Fe and Pt to form the $Fe_1(OH)_2O_2$@Pt(100) configuration. **(D)** Reaction of COOH on $Fe_1(OH)_2O_2$@Pt(100) to produce CO_2: **g,** COOH on $Fe_1(OH)_2O_2$@Pt(100); **h**, dehydrogenation of COOH to form CO_2 and $Fe_1(OH)_3O$@Pt(100); **i**, CO_2 releasing. **(E)** Reaction of CO with $Fe_1(OH)_3O$@Pt(100) to produce another CO_2: **j,** CO adsorption on the Pt atop sites; **k**, reaction of CO with the O atom in $Fe_1(OH)_3O$@Pt(100) to produce CO_2 and regenerate the initial $Fe_1(OH)_3$@Pt(100) structure. Here **ts-x-y** is the transition state of **x** to **y**. Fe, O, H, and Pt atoms are in orange, red, white, and blue, respectively.

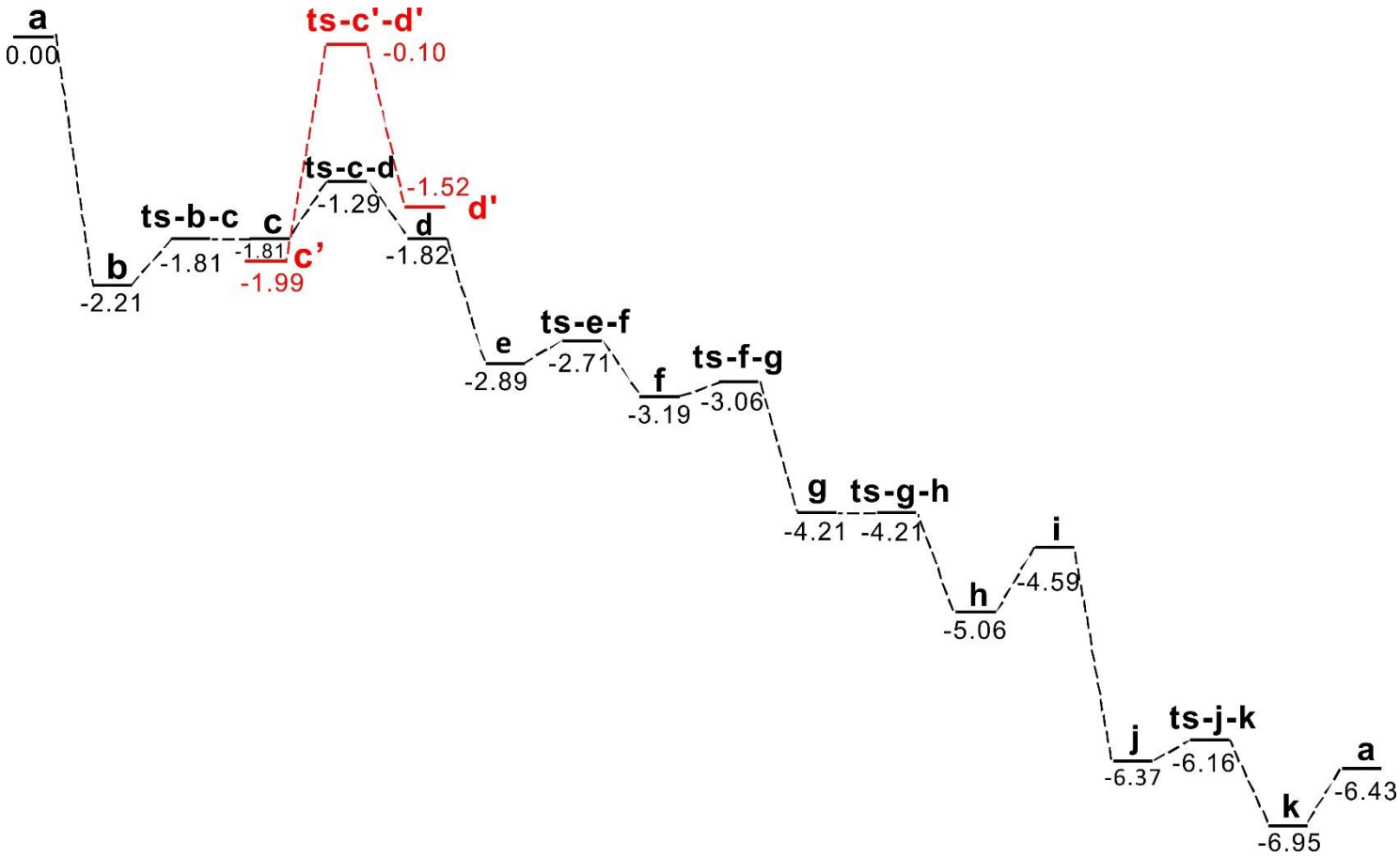

Supplementary Figure 37 | Energies of intermediates and transition states in $Fe_1(OH)_3$@Pt(100) catalyzed CO oxidation reaction. The energy values are in eV.

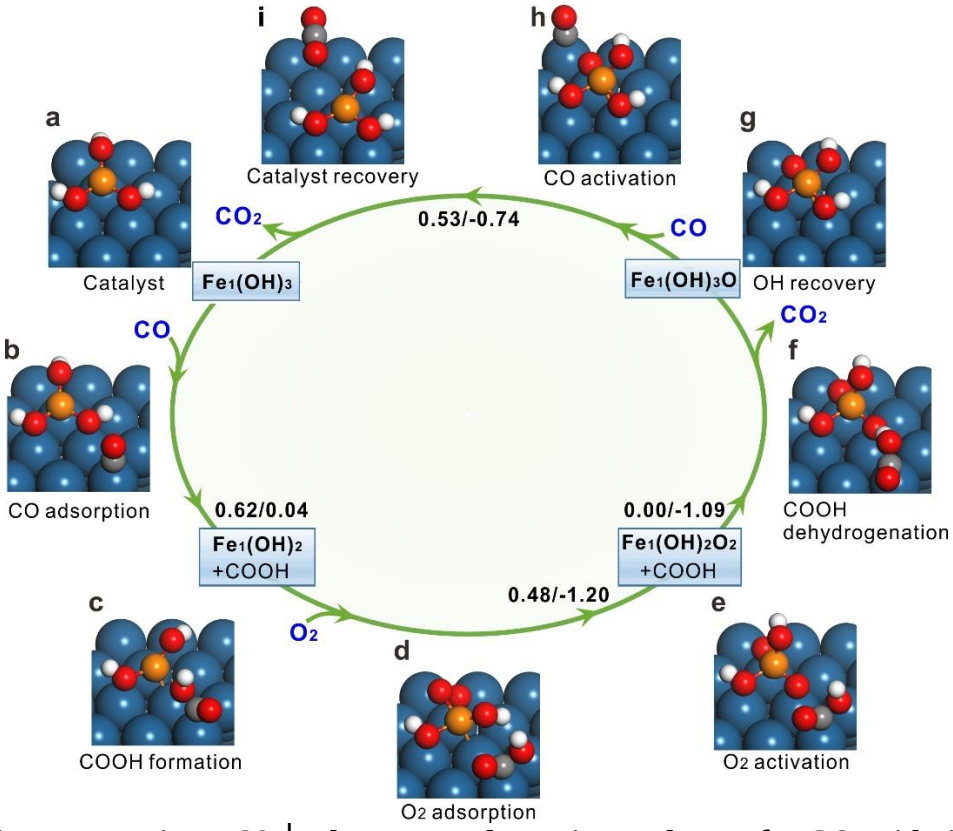

Supplementary Figure 38 | The proposed reaction pathways for CO oxidation on $Fe_1(OH)_3$@Pt(111). The structures of the key steps and intermediates are present (**a**-**h**). The energy barriers (left side of the slash) and reaction energies (right side of the slash) between the corresponding key steps are given in eV. Here Fe, O, H, and Pt atoms are in orange, red, white, and blue, respectively.

The detailed catalytic cycle of CO oxidation on $Fe_1(OH)_3$@Pt(111).

After CO chemisorption on the Pt atop site (Supplementary Fig. 38b), the adsorbed CO tends to attack one bridge-bonded OH group of $Fe_1(OH)_3$@Pt(111) to generate COOH* intermediate species on the Pt(111) surface. The step is almost neutral thermodynamically (E_r = 0.04) and the activation barrier is computed to be 0.62 eV (Supplementary Fig. 38c). The following steps are the adsorption and activation of molecular O_2 on the Fe atom to form the $Fe(OH)_2O_2$@Pt(111) structure (Supplementary Fig. 38d, e). The computed energy barrier for O_2 activation is 0.48 eV and the process is highly exothermic with a value of 1.20 eV. Next, the COOH* moiety transfers its H atom to $Fe(OH)_2O_2$@Pt(111) and generates $Fe(OH)_3O$@Pt(111) spontaneously without any barrier and exothermic by -1.09 eV (Supplementary Fig. 38g). After that, another CO adsorbs on the Pt surface and attacks the O atom of $Fe(OH)_3O$@Pt(111) to regenerate $Fe_1(OH)_3$@Pt(111) structure. The energy barrier is 0.53 eV and the reaction energy is -0.74 eV. The details of each step can be seen in Supplementary Fig. 39.

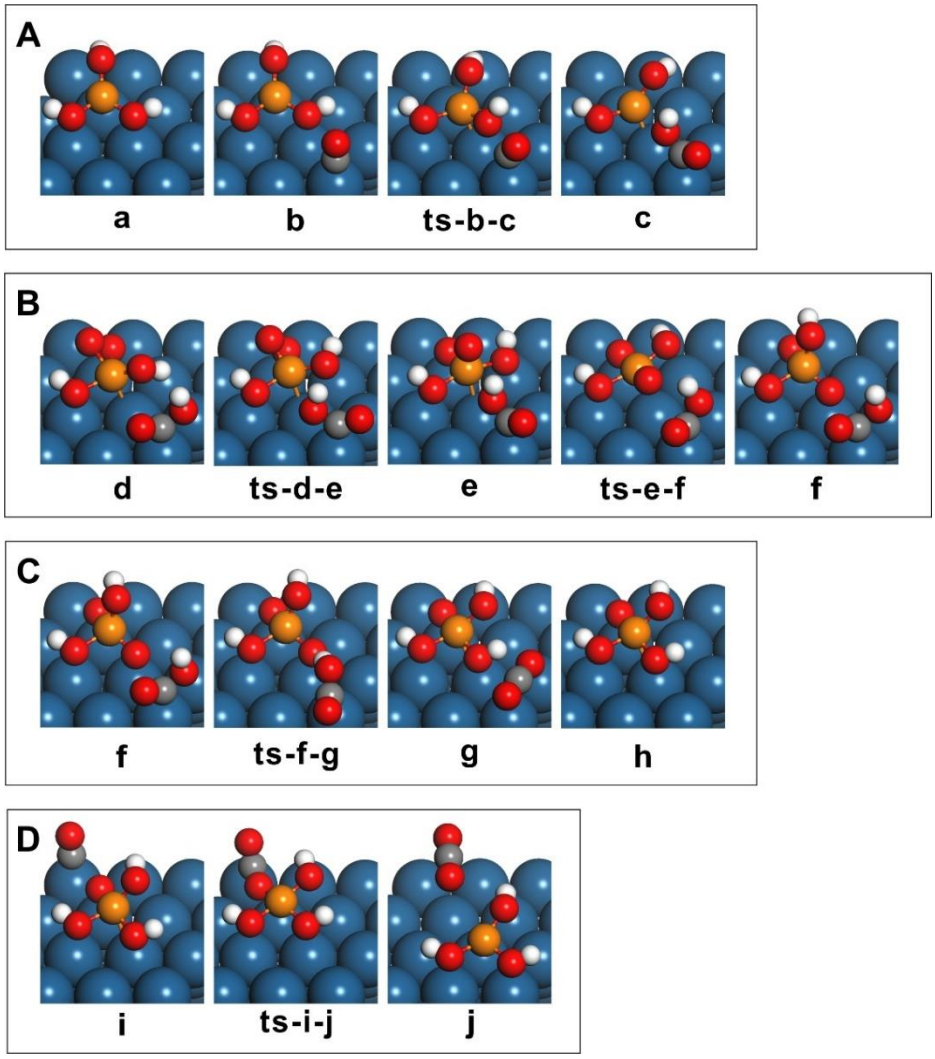

Supplementary Figure 39 | The detailed reaction steps involved in the CO oxidation on $Fe_1(OH)_3$@Pt(111). **(A)** CO chemisorption and association with the elongated OH group to form COOH species: **a,** the initial state of $Fe_1(OH)_3$@Pt(111); **b,** CO chemisorption at the atop sites of the Pt(111) surface; **c,** COOH formation by associating with the elongated OH group and forming $Fe_1(OH)_2$@Pt(111). **(B)** O_2 activation on $Fe_1(OH)_2$@Pt(111) configuration: **d,** O_2 adsorption on $Fe_1(OH)_2$@Pt(111) configuration; **e,** O_2 activation via one O flipping onto the Fe atop site of $Fe_1(OH)_2$@Pt(111); **f,** the O at the Fe atop sites flipped over to the bridge site between Fe and Pt to form the $Fe_1(OH)_2O_2$@Pt(111) configuration. **(C)** Reaction of COOH on $Fe_1(OH)_2O_2$@Pt(111) to produce CO_2: **f,** COOH on $Fe_1(OH)_2O_2$@Pt(111); **g,** dehydrogenation of COOH to form CO_2 and $Fe_1(OH)_3O$@Pt(111); **h,** CO_2 releasing. **(D)** Reaction of CO with $Fe_1(OH)_3O$@Pt(111) to produce another CO_2: **i,** CO adsorption on the Pt atop sites; **k,** reaction of CO with the O atom in $Fe_1(OH)_3O$@Pt(111) to produce CO_2 and regenerate the initial $Fe_1(OH)_3$@Pt(111) structure. Here **ts-x-y** is the transition state of **x** to **y**. Fe, O, H, and Pt atoms are in orange, red, white, and blue, respectively.

Supplementary Table 1 | Comparison of the catalytic performances over Pt-based catalysts with other Pt-based catalysts in the PROX reaction reported in literature.

Catalysts	Pt loadings (wt%)	Transition metal loadings (wt%)	Composition of feed gas (%)			Space velocity (mL $h^{-1}g_{cat}^{-1}$)	Maximal CO conversion (%)	Temperature window for the maximal CO conversion (K)		Notes
			CO	O_2	H_2			Temperature window	ΔT	
1cFe-Pt/SiO_2	3.6	0.10	1	0.5	48	36000	100	**~198-380**	**182**	This work
1cFe-Pt/SiO_2	3.6	0.10	1	0.6	48	36000	100	**~190-473**	**283**	This work
1cFe-Pt/SiO_2	3.6	0.10	1	0.7	48	36000	100	**~190-473**	**283**	This work
1cFe-Pt/SiO_2	3.6	0.10	1	0.8	48	36000	100	**~190-473**	**283**	This work
1cFe-Pt/SiO_2	3.6	0.10	1	1	48	36000	100	**~190-473**	**283**	This work
2cFe-Pt/SiO_2	3.6	0.19	1	0.5	48	36000	100	**~200-380**	**180**	This work
3cFe-Pt/SiO_2	3.6	0.27	1	0.5	48	36000	100	**~200-380**	**180**	This work
5cFe-Pt/SiO_2	3.6	0.44	1	0.5	48	36000	100	**~215-310**	**95**	This work
10cFe-Pt/SiO_2	3.6	0.66	1	0.5	48	36000	100	**~280-310**	**30**	This work
Pt-Fe/SiO_2	4	0.5	1	0.5	98.5	36000	100	**~300-320**	**20**	Ref [17]
Pt-Fe/SiO_2	1	0.11	0.5	0.5	45	120000	~98	**~423**	**0**	Ref [29]
Pt-Fe/Al_2O_3	0.71	0.23	1	1	50	20000	100	**~298-353**	**55**	Ref [30]
Pt-Fe/Al_2O_3	3	1.72	2	1	40	40000	50	**~373**	**0**	Ref [31]
Pt-Fe/γ-Al_2O_3	1	2.87	1	1	10	60000	95	**~350**	**0**	Ref [32]

Pt-Fe/γ-Al_2O_3	1	2.87	1	1	80	60000	55	**~370**	**0**	Ref [32]
Pt–Fe/zeolite	4	2	1	0.5	98.5	120000	100	**~353-473**	**120**	Ref [33]
Pt–Fe/zeolite	4	2	1	0.5	78.5	120000	100	**~423-473**	**50**	Ref [33]
Pt–Fe/zeolite	4	2	1	0.5	53.5	120000	100	**~348-423**	**75**	Ref [33]
Pt-Fe/mordenite	4	0.5	1	1	98.5	95000	100	**~373-423**	**50**	Ref [34]
FeO_x/Pt/TiO_2	1	50	3	1.5	20	4000	95	**~323**	**0**	Ref [35]
Pt-Fe/Carbon black	4	0.3	1	0.5	50	30000	100	**~303-318**	**15**	Ref [18]
Cu@Pt-Fe-Carbon black	0.9	0.5	1	0.5	50	30000	100	**~303-313**	**10**	Ref [36]
Pt/Fe_2O_3	2.5	97.5	1	1	40	18750	100	**~293-343**	**50**	Ref [37]
Pt-Co/Carbon black	4	0.5	1	0.5	50	30000	100	**~313**	**0**	Ref[38]
Pt-Co/YSZ	0.5	0.76	1	1	80	60000	100	**~380**	**0**	Ref [39]
Pt-Co/CNTs	4	0.7	1	1	50	30000	100	**~313-433**	**120**	Ref [40]
Pt-Co/CoAPO-5	1	2	1	1	50	24000	100	**~338-383**	**45**	Ref [41]
Pt-Co/SiO_2	3	0.3	2	2	35	162000	100	**~393**	**0**	Ref [42]
Pt-Co/SiO_2	3	0.3	2	1.5	35	168000	100	**~453**	**0**	Ref [43]
Pt-Co/TiO_2	1.44	3.32	1	1.25	97.75	47143	100	**~298**	**0**	Ref [44]
Pt-Co/MgO	3	0.3	2	2	35	162000	100	**~393-433**	**40**	Ref [42]

Pt-Co/Al_2O_3	3	0.3	2	2	35	162000	98	**~433**	**0**	Ref [42]
Pt-Co/Al_2O_3	1	3	1.1	2	67	40000	100	**~393**	**0**	Ref [45]
Pt-Co/γ-Al_2O_3	1	3.03	1	1	10	60000	100	**~390**	**0**	Ref [32]
Pt-Co/γ-Al_2O_3	1	3.03	1	1	80	60000	80	**~390**	**0**	Ref [32]
Pt-Co/La_2O_3	3	0.3	2	2	35	162000	40	**~433**	**0**	Ref [42]
Pt-Co/CaO	3	0.3	2	2	35	162000	30	**~433**	**0**	Ref [42]
Pt-Cu/Al_2O_3	3	1	2	2	22	168000	97	**~400**	**0**	Ref [46]
Pt-Cu/CeO_2	2.69	1.04	1	2	60	25000	100	**~363-433**	**70**	Ref [47]
Pt-Cu/γ-Al_2O_3	1	3.28	1	1	10	60000	100	**~350-390**	**40**	Ref [32]
Pt-Cu/γ-Al_2O_3	1	3.28	1	1	80	60000	95	**~350**	**0**	Ref [32]
Pt-Ni/γ-Al_2O_3	1	3.03	1	1	10	60000	100	**~395-415**	**20**	Ref [32]
Pt-Ni/γ-Al_2O_3	1	3.03	1	1	80	60000	85	**~375**	**0**	Ref [32]
Pt-Ni/γ- Al_2O_3	1	1.5	1	1	50	60000	100	**~402-410**	**8**	Ref [48]
Pt-Pd/CeO_2	0.125	0.875 (Pd)	1	0.5	40	30000	77	**~383**	**0**	Ref [49]
Pt-Re/SiO_2	2	0.95	1	1.25	60	90909	100	**~360-440**	**80**	Ref [50]
Pt-Zr/γ-Al_2O_3	1	4.67	1	1	10	60000	95	**~475-500**	**25**	Ref [32]
Pt-Cr/γ-Al_2O_3	1	2.67	1	1	10	60000	80	**~440**	**0**	Ref [32]
Pt-Zn/γ-Al_2O_3	1	3.33	1	1	10	60000	95	**~450**	**0**	Ref [32]

Pt-Mn/γ-Al_2O_3	1	2.82	1	1	10	60000	100	**~395**	**0**	Ref [32]
Pt-Ce/γ-Al_2O_3	1	7.18	1	1	10	60000	90	**~350**	**0**	Ref [32]
MnO_x/Pt/Al_2O_3	0.38	10.56	1	3	60	12000	100	**~438-503**	**65**	Ref [51]
K–Pt/Al_2O_3	2	--	0.2	0.2	75	30000	100	**~360-450**	**90**	Ref [52]
Pt/SiO_2	3.6	--	1	0.5	48	36000	~80	**~427-473**	**46**	This work
Pt/SiO_2	1	--	0.5	0.5	45	120000	95	**500**	**0**	Ref [29]
Pt/SiO_2	4	--	1	0.5	98.5	36000	70	**473**	**0**	Ref [17]
Pt/Mesoporous Silica	5	--	1	1	93	12000	100	**~423**	**0**	Ref [53]
Pt/Mesoporous Silica	5	--	1	0.5	93.5	12000	100	**~333-423**	**90**	Ref [53]
Pt/TiO_2	1	--	0.5	0.5	45	120000	75	**523**	**0**	Ref [54]
Pt/γ-Al_2O_3	1	--	0.5	0.5	45	120000	100	**~473**	**0**	Ref [54]
Pt/γ-Al_2O_3	1	--	1	1	10	60000	100	**~450**	**0**	Ref [32]
Pt/γ-Al_2O_3	1	--	1	1	80	60000	70	**~475**	**0**	Ref [32]
Pt/Al_2O_3	0.72	-	1	1	50	20000	~73	**473**	**0**	Ref [30]

Supplementary Table 2 | Catalytic performances of Ir-based or Ru-based catalysts in the PROX reaction reported in literature.

Catalysts	Ir (or Ru) loadings (wt%)	Transition metal loadings (wt%)	Composition of feed gas (%)			Space velocity (mL $h^{-1}g_{cat}^{-1}$)	Maximal CO conversion (%)	Temperature window for the maximal CO conversion (K)		Notes
			CO	O_2	H_2			Temperature window	ΔT	
$Ir/Fe(OH)_x$	2.4		1	1	40	18000	100	**~293-333**	**40**	Ref [55]
$Ir\text{-}Fe/SiO_2$	3	4.4	2	1	10	40000	85	**~373-393**	**20**	Ref [56]
Ru/ZSM5	1	--	1	1	98	9600-96000	88	**~413**	**0**	Ref [57]
Ru/ZSM5	1	--	1	1	98	9600-96000	98	**~398**	**0**	Ref [57]
Ru/SiO_2	1	--	1	1	98	9600-96000	65	**~413**	**0**	Ref [57]
Ru/Al_2O_3	1	--	1	1	98	9600-96000	60	**~423**	**0**	Ref [57]
Ru/CeO_2	1	--	1	1	98	9600-96000	50	**~373**	**0**	Ref [57]

Supplementary Table 3 | Catalytic performances of Au-based catalysts in the PROX reaction reported in literature.

Catalysts	Au loadings (wt%)	Composition of feed gas (%)			Space velocity (mL $h^{-1}g_{cat}^{-1}$)	Maximal CO conversion (%)	Temperature window for the maximal CO conversion (K)		Notes
		CO	O_2	H_2			Temperature window	ΔT	
Au/Fe_2O_3	4.4	1	1	40	18750	100	**~293-313**	**20**	Ref [37]
Au/CeO_2	1	2	1	50	60000	65	**~453**	**0**	Ref [58]
Au_1/CeO_2 (single atom)	0.05	1	1	40	25000	100	**~343-393**	**50**	Ref[59]
Au/CeZr10	1	2	1	50	60000	66	**~343**	**0**	Ref [58]
Au/CeZn10	1.1	2	1	50	60000	74	**~343**	**0**	Ref [58]
Au/CeFe10	0.9	2	1	50	60000	74	**~343**	**0**	Ref [58]
Au/CeO_2-rods	0.92	1	1	50	30000	90	**~360-390**	**30**	Ref [60]
Au/CeO_2-polyhedra	0.83	1	1	50	30000	70	**~380**	**0**	Ref [60]
Au/CeO_2-cubes	0.92	1	1	50	30000	55	**~390**	**0**	Ref [60]
AuCeFeMA	3	0.3	0.3	50	60000	100	**~298-348**	**50**	Ref [61]
AuCeMnMA	3	0.3	0.3	50	60000	95	**~373**	**0**	Ref [61]

Supplementary Table 4 | Catalytic performances of Cu-based catalysts in the PROX reaction reported in literature.

Catalysts	Cu loadings (wt%)	Composition of feed gas (%)			Space velocity (mL $h^{-1}g_{cat}^{-1}$)	Maximal CO conversion (%)	Temperature window for the maximal CO conversion (K)		Notes
		CO	O_2	H_2			Temperature window	ΔT	
$CuO\text{-}CeO_2$	16	1	1	50	60000	100	**~388-445**	**57**	Ref [62]
$CuO\text{-}CeO_2$	3.2	0.5	0.5	50	156522	100	**~413-453**	**40**	Ref [63]
$Cu\text{-}CeO_2$	20	1	1	50	120000	~100	**~393–448**	**55**	Ref [64]
$Cu\text{-}CeO_2$	16	1	1.25	50	120000	~100	**~448**	**0**	Ref [65]
$7\%CuO/Ce_{0.9}Zr_{0.1}O_2\text{-}Al_2O_3$	7	1	1	50	10000	~100	**~373-403**	**30**	Ref [66]
$5\%CuO/20\%CeO_2/\gamma\text{-}Al_2O_3$	5	0.6	0.6	30	18000	99	**~473**	**0**	Ref [67]

Supplementary Table 5 | Comparison of catalytic performances of Pt- Au- and Ir-based catalysts in the PROX reaction reported in literature.

Catalysts	Noble metal loadings (wt%)	Temperature (K)	TOF (s^{-1})	Mass specific rate ($Mol_{CO}\ g_m^{-1}\ h^{-1}$)[d]	Notes
1cFe-Pt/SiO_2	3.6 (0.10[a])	200	0.65[b] (0.14[c])	1.17	This work
		300	2.10[b] (0.46[c])	5.21	
		350	5.85[b]	10.4	
2cFe-Pt/SiO_2	3.6 (0.19[a])	200	0.52[b] (0.25[c])	1.80	This work
		300	1.02[b] (0.48[c])	5.61	
3cFe-Pt/SiO_2	3.6 (0.27[a])	200	0.32[b] (0.25[c])	1.52	This work
		300	0.72[b] (0.57[c])	5.34	
Pt/SiO_2	3.6	300	7.3×10^{-4},[c]	0.06	This work
Pt/Fe_2O_3	4.0	300	0.16[c]	0.18	This work
Pt/Al_2O_3	2.0	353	2.0×10^{-3}	-	Ref [52]
Pt_1/FeO_x (Single atoms)	0.17	300	0.21	0.68	Ref [68]
Pt/FeO_x-C2	2.0	300	0.14	0.26	Ref [37]
Pt-Co/Carbon black	4.0	313	0.1	-	Ref[38]
Au_1/CeO_2 (single atoms)	0.05	313	-	1.1	Ref[59]
Au_1/CeO_2 (single atoms)	0.05	353	2.5	45.9	Ref[59]
Au/Fe_2O_3	4.4	300	0.09	0.39	Ref [37]
Ir/$Fe(OH)_x$	2.4	300	0.1	0.48	Ref [55]

[a]Fe loadings; [b]TOF was calculated based on the Fe loadings, since the number of active sites is equal to the mole of Fe in the sample owing to the selective FeO_x ALD; [c]TOF was calculated based the number of Pt surface atoms, determined by CO chemisorption measurements; [d]m is Pt, Au or Ir.

Supplementary Table 6 | Structural parameters at the Fe K-edge extracted from quantitative EXAFS curve-fittings using the ARTEMIS module of IFEFFIT. For comparison, the interatomic distances and coordination numbers for the references (Fe foil, FeO, Fe_2O_3 and FeOOH) calculated from their crystallographic structures are also listed.

Sample	Path	CNs	*R* (Å)	σ^2 (10^{-3}Å^2)	ΔE_0 (eV)
Fe foil[69]	Fe-Fe	8.0	2.48		
	Fe-Fe	6.0	2.87		
FeO[70]	Fe-O	6.0	2.16		
	Fe-Fe	12.0	3.06		
Fe_2O_3[71]	Fe-O	3.0	1.94		
	Fe-O	3.0	2.11		
	Fe-Fe	1.0	2.90		
	Fe-Fe	3.0	2.97		
	Fe-Fe	3.0	3.36		
	Fe-Fe	6.0	3.70		
FeOOH[72]	Fe-O	2.0	1.98		
	Fe-O	2.0	2.01		
	Fe-O	2.0	2.07		
	Fe-Fe	4.0	3.06		
	Fe-Fe	2.0	3.07		
0.4cFe-Pt/SiO_2-O	Fe-O	5.2±0.8	1.94±0.01	9.4±1.5	-6.4±1.5
1cFe-Pt/SiO_2-O	Fe-O	5.6±0.8	1.93±0.01	9.5±1.5	-7.0±1.5
3cFe-Pt/SiO_2-O	Fe-O	5.0±0.8	1.94±0.01	9.7±1.5	-5.2±1.5
10cFe-Pt/SiO_2-O	Fe-O	5.7±0.8	1.95±0.01	9.5±1.5	-5.5±1.5
0.4cFe-Pt/SiO_2-R	Fe-O	2.0±0.4	1.99±0.02	10.8±2.1	-4.4±2.4
	Fe-Pt	4.2±0.8	2.60±0.03	10.6±2.1	-7.5±2.0
	Fe-Fe	0.3±0.2	3.11±0.06	10.6±2.1	-7.5±2.0
1cFe-Pt/SiO_2-R	Fe-O	1.9±0.4	1.98±0.02	9.8±2.0	-6.2±2.8
	Fe-Pt	4.1±0.8	2.61±0.03	10.3±2.1	-6.2±1.8
	Fe-Fe	0.3±0.2	3.09±0.06	10.3±2.1	-6.2±1.8
3cFe-Pt/SiO_2-R	Fe-O	1.2±0.3	1.93±0.02	10.4±2.0	-6.3±2.7
	Fe-O	1.7±0.4	2.01±0.02	10.4±2.0	-6.3±2.7
	Fe-Pt	4.2±0.8	2.62±0.03	10.1±1.9	-9.4±2.1
	Fe-Fe	0.4±0.2	2.85±0.05	10.1±2.6	-6.2*
	Fe-Fe	0.6±0.2	3.10±0.06	10.1±2.4	-6.2*
10cFe-Pt/SiO_2-R	Fe-O	1.8±0.4	1.94±0.02	12.5±2.0	-2.4±1.0
	Fe-O	1.3±0.3	2.01±0.03	12.5±2.0	-2.4±1.0
	Fe-Pt	2.6±0.5	2.59±0.03	9.4±1.6	-8.3±2.8
	Fe-Fe	1.2±0.3	2.86±0.06	9.4±1.4	-6.2*
	Fe-Fe	1.3±0.2	3.10±0.06	9.4±1.4	-6.2*

0.4cFe-Pt/SiO_2-R(473K)	Fe-O	1.8±0.4	1.99±0.02	10.3±1.7	-2.8±1.8
	Fe-Pt	4.3±0.8	2.62±0.03	10.2±2.0	-5.1±1.7
	Fe-Fe	0.3±0.2	3.08±0.06	10.2±2.0	-5.1±1.7
1cFe-Pt/SiO_2-R(473K)	Fe-O	2.0±0.4	1.99±0.02	10.4±2.1	-4.1±2.0
	Fe-Pt	4.3±0.8	2.62±0.03	10.4±2.1	-4.9±1.9
	Fe-Fe	0.3±0.2	3.10±0.06	10.4±2.5	-4.9±1.9
3cFe-Pt/SiO_2-R(473K)	Fe-O	1.3±0.3	1.91±0.02	9.5±2.0	-8.5±2.0
	Fe-O	0.9±0.2	1.99±0.02	9.5±2.0	-8.5±2.0
	Fe-Pt	3.8±0.7	2.58±0.03	9.5±2.1	-9.8±2.7
	Fe-Fe	0.3±0.2	2.85±0.06	9.5±2.1	-6.2*
	Fe-Fe	0.4±0.2	3.06±0.06	9.5±2.1	-6.2*
10cFe-Pt/SiO_2-R(473K)	Fe-O	1.5±0.3	1.94±0.02	11.0±2.2	-7.9±2.1
	Fe-O	1.5±0.3	2.02±0.02	11.0±2.2	-7.9±2.1
	Fe-Pt	2.9±0.5	2.63±0.03	9.7±2.0	-8.1±2.4
	Fe-Fe	0.9±0.2	2.90±0.05	9.7±2.6	-6.2*
	Fe-Fe	1.0±0.2	3.10±0.05	9.7±2.6	-6.2*
1cFe-Pt/SiO_2-P	Fe-O	2.0±0.4	1.96±0.02	9.7±2.0	2.0±1.3
	Fe-O	1.0±0.2	2.01±0.03	11.0±2.2	2.0±1.3
	Fe-Pt	1.0±0.2	2.59±0.03	11.0±2.2	-4.5±2.0
	Fe-Pt	3.0±0.6	2.67±0.03	12.0±2.4	-4.5±2.0
	Fe-Fe	0.4±0.2	2.90±0.06	10.6±2.1	-1.6±1.0

CNs, coordination numbers; R, bonding distance; $\Delta\sigma^2$, Debye-Waller factor; ΔE_0, inner potential shift; *This parameter is fixed.

Supplementary Table 7 | Structural parameters at the Pt L_3-edge extracted from quantitative EXAFS curve-fittings using the ARTEMIS module of IFEFFIT. For comparison, the interatomic distances and coordination numbers for the references (Pt foil and PtO_2) calculated from their crystallographic structures are also listed.

Sample	Path	CNs	*R* (Å)	σ^2 (10^{-3}Å^2)	ΔE_0 (eV)
Pt foil[73]	Pt-Pt	12.0	2.77		
PtO_2[74]	Pt-O	6.0	2.07		
	Pt-Pt	6.0	3.10		
	Pt-O	6.0	3.60		
	Pt-O	6.0	3.73		
1cFe-Pt/SiO_2-O	Pt-O	2.0±0.4	2.04±0.02	6.0±1.2	7.6±2.2
	Pt-Pt	6.5±1.3	2.73±0.02	11.0±2.2	6.0±1.5
	Pt-Pt	2.0±0.4	3.06±0.02	12.0±2.4	6.0±1.5
1cFe-Pt/SiO_2-R	Pt-Fe	0.6±0.2	2.63±0.03	6.7±1.3	6.0±1.5
	Pt-Pt	9.9±1.0	2.75±0.02	7.4±1.5	7.3±2.0
1cFe-Pt/SiO_2-P	Pt-Fe	0.7±0.2	2.63±0.03	6.7±1.3	5.0±1.5
	Pt-Pt	9.8±1.0	2.75±0.02	7.4±1.5	6.5±1.7

CNs, coordination numbers; R, bonding distance; σ^2, Debye-Waller factor; ΔE_0, inner potential shift.

Supplementary Table 8 | Structural parameters of $Fe_1(OH)_3$@Pt(100) model by DFT calculations.

Sample	Metal	Shell	*R* (Å)		
$Fe_1(OH)_3$@Pt(100)	Pt	Pt-Pt	2.80[a]	2.77[b]	2.75[c]
	Fe	Fe-O_1	1.93[a]	1.94[b]	1.93[c]
		Fe-O_1	1.94[a]	1.95[b]	1.94[c]
		Fe-O_2	2.00[a]	2.00[b]	2.00[c]
		Fe-Pt_1	2.60[a]	2.60[b]	2.60[c]
		Fe-Pt_2	2.70[a]	2.69[b]	2.68[c]
		Fe-Pt_2	2.70[a]	2.70[b]	2.70[c]
		Fe-Pt_2	2.71[a]	2.71[b]	2.70[c]
$Fe_1(OH)_3$@Pt(111)	Fe	Fe-O_1	1.95[a]		
		Fe-O_1	1.95[a]		
		Fe-O_2	1.80[a]		
		Fe-Pt_1	2.51[a]		
		Fe-Pt_2	2.95[a]		
		Fe-Pt_2	2.98[a]		

[a]The calculated data at the computational level.
[b]The normalized bond distance after fixing the Pt-Pt distance to 2.77 Å as in Pt bulk material.
[c]The normalized bond distance after fixing the Pt-Pt distance to 2.75 Å as measured by in situ EXAFS on the 1cFe-Pt/SiO_2 sample under the PROX conditions.

References

1 Rooth, M. *et al.* Atomic layer deposition of iron oxide thin films and nanotubes using ferrocene and oxygen as precursors. *Chem. Vap. Deposition* **14**, 67-70 (2008).

2 Scheffe, J. R. *et al.* Atomic layer deposition of iron(III) oxide on zirconia nanoparticles in a fluidized bed reactor using ferrocene and oxygen. *Thin Solid Films* **517**, 1874-1879 (2009).

3 Nyholm, R., Andersen, J. N., Johansson, U., Jensen, B. N. & Lindau, I. Beamline I311 at MAX-LAB: a VUV/soft X-ray undulator beamline for high resolution electron spectroscopy. *Nuclear Instruments and Methods in Physics Research Section A: Accelerators, Spectrometers, Detectors and Associated Equipment* **467–468, Part 1**, 520-524 (2001).

4 Wang, W. *et al.* Observation of water dissociation on nanometer-sized FeO islands grown on Pt(111). *Chem. Phys. Lett.* **500**, 76-81 (2010).

5 Kresse, G. & Furthmuller, J. Efficiency of ab-initio total energy calculations for metals and semiconductors using a plane-wave basis set. *Comp. Mater. Sci.* **6**, 15-50 (1996).

6 Kresse, G. & Furthmüller, J. Efficient iterative schemes forab initiototal-energy calculations using a plane-wave basis set. *Phys. Rev. B* **54**, 11169-11186 (1996).

7 Blochl, P. E. Projector Augmented-Wave Method. *Phys. Rev. B* **50**, 17953-17979 (1994).

8 Kresse, G. & Joubert, D. From ultrasoft pseudopotentials to the projector augmented-wave method. *Phys. Rev. B* **59**, 1758-1775 (1999).

9 Klimeš, J., Bowler, D. R. & Michaelides, A. Van der Waals density functionals applied to solids. *Phys. Rev. B* **83**, 195131 (2011).

10 Klimes, J., Bowler, D. R. & Michaelides, A. Chemical accuracy for the van der Waals density functional. *J. Phys.: Condens. Matter* **22**, 022201 (2010).

11 Monkhorst, H. J. & Pack, J. D. Special points for Brillouin-zone integrations. *Phys. Rev. B* **13**, 5188-5192 (1976).

12 Henkelman, G., Uberuaga, B. P. & Jónsson, H. A climbing image nudged elastic band method for finding saddle points and minimum energy paths. *J. Chem. Phys.* **113**, 9901 (2000).

13 Zhang, W. H., Carravetta, V., Li, Z. Y., Luo, Y. & Yang, J. L. Oxidation states of graphene: Insights from computational spectroscopy. *J. Chem. Phys.* **131** (2009).

14 Butcher, D. R. *et al.* In Situ Oxidation Study of Pt(110) and Its Interaction with CO. *J. Am. Chem. Soc.* **133**, 20319-20325 (2011).

15 Newton, M. A., Ferri, D., Smolentsev, G., Marchionni, V. & Nachtegaal, M. Room-temperature carbon monoxide oxidation by oxygen over Pt/Al2O3 mediated by reactive platinum carbonates. *Nat. Commun.* **6** (2015).

16 Newton, M. A., Ferri, D., Smolentsev, G., Marchionni, V. & Nachtegaal, M. Kinetic Studies of the Pt Carbonate-Mediated, Room-Temperature Oxidation of Carbon Monoxide by Oxygen over Pt/Al2O3 Using Combined, Time-Resolved XAFS, DRIFTS, and Mass Spectrometry. *J. Am. Chem. Soc.* **138**, 13930-13940 (2016).

17 Fu, Q. *et al.* Interface-confined ferrous centers for catalytic oxidation. *Science* **328**, 1141-1144 (2010).

18 Xu, H., Fu, Q., Yao, Y. & Bao, X. Highly active Pt–Fe bicomponent catalysts for CO oxidation in the presence and absence of H_2. *Energy Environ. Sci.* **5**, 6313-6320 (2012).

19 Chen, G. X. *et al.* Interfacial Effects in Iron-Nickel Hydroxide-Platinum Nanoparticles Enhance Catalytic Oxidation. *Science* **344**, 495-499 (2014).

20 Ringleb, F. *et al.* Interaction of Water with FeO(111)/Pt(111): Environmental Effects and Influence of Oxygen. *J. Phys. Chem. C* **115**, 19328-19335 (2011).

21 Wei, M. M., Fu, Q., Dong, A. Y., Wang, Z. J. & Bao, X. H. Coverage and Substrate Effects on the Structural Change of FeOx Nanostructures Supported on Pt. *Top. Catal.* **57**, 890-898 (2014).

22 Braun, K. F., Iancu, V., Pertaya, N., Rieder, K. H. & Hla, S. W. Decompositional incommensurate growth of ferrocene molecules on a Au(111) surface. *Phys. Rev. Lett.* **96**, 246102 (2006).

23 Paul, R., Reifenberger, R. G., Fisher, T. S. & Zemlyanov, D. Y. Atomic Layer Deposition of FeO on Pt(111) by Ferrocene Adsorption and Oxidation. *Chem. Mater.* **27**, 5915-5924 (2015).

24 Ma, Q., Guo, H. S., Gordon, R. G. & Zaera, F. Uptake of Copper Acetamidinate ALD Precursors on Nickel Surfaces. *Chem. Mater.* **22**, 352-359 (2010).

25 Ma, Q., Guo, H. S., Gordon, R. G. & Zaera, F. Surface Chemistry of Copper(I) Acetamidinates in Connection with Atomic Layer Deposition (ALD) Processes. *Chem. Mater.* **23**, 3325-3334 (2011).

26 Masango, S. S., Peng, L. X., Marks, L. D., Van Duyne, R. P. & Stair, P. C. Nucleation and Growth of Silver Nanoparticles by AB and ABC-Type Atomic Layer Deposition. *J. Phys. Chem. C* **118**, 17655-17661 (2014).

27 Lu, J. L. *et al.* First-Principles Predictions and in Situ Experimental Validation of Alumina Atomic Layer Deposition on Metal Surfaces. *Chem. Mater.* **26**, 6752 (2014).
28 Lu, J. L. & Elam, J. W. Low Temperature ABC-Type Ru Atomic Layer Deposition through Consecutive Dissociative Chemisorption, Combustion, and Reduction Steps. *Chem. Mater.* **27**, 4950-4956 (2015).
29 Siani, A. *et al.* Improved CO oxidation activity in the presence and absence of hydrogen over cluster-derived PtFe/SiO_2 catalysts. *Langmuir* **22**, 5160-5167 (2006).
30 Zhang, H. *et al.* Construction of ultrafine and stable PtFe nano-alloy with ultra-low Pt loading for complete removal of CO in PROX at room temperature. *Appl. Catal. B-Environ.* **180**, 237-245 (2016).
31 Yin, J., Wang, J., Zhang, T. & Wang, X. Novel Alumina-Supported PtFe Alloy Nanoparticles for Preferential Oxidation of Carbon Monoxide in Hydrogen. *Catal. Lett.* **125**, 76-82 (2008).
32 Ko, E. Y. *et al.* Selective CO oxidation in the presence of hydrogen over supported Pt catalysts promoted with transition metals. *Korean J. Chem. Eng.* **23**, 182-187 (2006).
33 Watanabe, M., Uchida, H., Ohkubo, K. & Igarashi, H. Hydrogen purification for fuel cells: selective oxidation of carbon monoxide on Pt-Fe/zeolite catalysts. *Appl. Catal. B Environ.* **46**, 595-600 (2003).
34 Maeda, N., Matsushima, T., Uchida, H., Yamashita, H. & Watanabe, M. Performance of Pt-Fe/mordenite monolithic catalysts for preferential oxidation of carbon monoxide in a reformate gas for PEFCs. *Appl. Catal. A Gen.* **341**, 93-97 (2008).
35 Tanaka, K.-I., Shou, M., He, H. & Shi, X. Significant enhancement of the oxidation of CO by H_2 and/or H_2O on a FeO_x/Pt/TiO_2 catalyst. *Catal. Lett.* **110**, 185-190 (2006).
36 Guo, X. *et al.* Ferrous centers confined on core-shell nanostructures for low-temperature CO oxidation. *J. Am. Chem. Soc.* **134**, 12350-12353 (2012).
37 Qiao, B. T. *et al.* Ferric Oxide-Supported Pt Subnano Clusters for Preferential Oxidation of CO in H_2-Rich Gas at Room Temperature. *ACS Catal.* **4**, 2113-2117 (2014).
38 Xu, H., Fu, Q., Guo, X. G. & Bao, X. H. Architecture of Pt-Co Bimetallic Catalysts for Catalytic CO Oxidation. *Chemcatchem* **4**, 1645-1652 (2012).
39 Ko, E. Y., Park, E. D., Lee, H. C., Lee, D. & Kim, S. Supported Pt-Co catalysts for selective CO oxidation in a hydrogen-rich stream. *Angew. Chem. Int. Ed.* **46**, 734-737 (2007).
40 Wang, C., Li, B., Lin, H. & Yuan, Y. Carbon nanotube-supported Pt-Co bimetallic catalysts for preferential oxidation of CO in a H_2-rich stream with CO_2 and H_2O vapor. *J. Power Sources* **202**, 200-208 (2012).
41 Wang, C., Zhang, L. & Liu, Y. Aluminumphosphate molecular sieves supported Pt–Co catalysts for the preferential oxidation of CO in H_2-rich gases. *Appl. Catal. B Environ.* **136-137**, 48-55 (2013).
42 Furukawa, S., Ehara, K. & Komatsu, T. Unique reaction mechanism of preferential oxidation of CO over intermetallic Pt_3Co catalysts: surface-OH-mediated formation of a bicarbonate intermediate. *Catal. Sci. Technol.* **6**, 1642-1650 (2016).
43 Komatsu, T. & Tamura, A. Pt3Co and PtCu intermetallic compounds: Promising catalysts for preferential oxidation of CO in excess hydrogen. *J. Catal.* **258**, 306-314 (2008).
44 Epling, W. S., Cheekatamarla, P. K. & Lane, A. M. Reaction and surface characterization studies of titania-supported Co, Pt and Co/Pt catalysts for the selective oxidation of CO in H_2-containing streams. *Chem. Eng. J.* **93**, 61-68 (2003).
45 Yan, J., Ma, J. X., Cao, P. & Li, P. Preferential oxidation of CO in H_2-rich gases over Co-promoted Pt-gamma-Al_2O_3 catalyst. *Catal. Lett.* **93**, 55-60 (2004).
46 Komatsu, T., Takasaki, M., Ozawa, K., Furukawa, S. & Muramatsu, A. PtCu Intermetallic Compound Supported on Alumina Active for Preferential Oxidation of CO in Hydrogen. *J. Phys. Chem. C* **117**, 10483-10491 (2013).
47 Kugai, J. *et al.* Structure and Catalytic Performance of Pt–Cu Bimetallic Catalysts Synthesized by a Radiation-Induced Reduction Method in the Aqueous Phase: Influence of Support Material and Sulfate Ion in the Precursor. *J. Phys. Chem. C* **117**, 5742-5751 (2013).
48 Ko, E.-Y. *et al.* Pt–Ni/γ-Al_2O_3 catalyst for the preferential CO oxidation in the hydrogen stream. *Catal. Lett.* **110**, 275-279 (2006).
49 Parinyaswan, A., Pongstabodee, S. & Luengnaruemitchai, A. Catalytic performances of Pt–Pd/CeO_2 catalysts for selective CO oxidation. *Int. J. Hydrogen Energy* **31**, 1942-1949 (2006).
50 Ebashi, T. *et al.* Preferential CO Oxidation in a H_2-Rich Stream on Pt-ReO_x/SiO_2: Catalyst Structure and Reaction Mechanism. *J. Phys. Chem. C* **114**, 6518-6526 (2010).
51 Ayastuy, J. L., González-Marcos, M. P., González-Velasco, J. R. & Gutiérrez-Ortiz, M. A. MnO_x/Pt/Al_2O_3 catalysts for CO oxidation in H_2-rich streams. *Appl. Catal. B Environ.* **70**, 532-

541 (2007).
52 Minemura, Y. *et al.* Preferential CO oxidation promoted by the presence of H_2 over K-Pt/Al_2O_3. *Chem. Commun.*, 1429-1431 (2005).
53 Fukuoka, A., Kimura, J. I., Oshio, T., Sakamoto, Y. & Ichikawa, M. Preferential oxidation of carbon monoxide catalyzed by platinum nanoparticles in mesoporous silica. *J. Am. Chem. Soc.* **129**, 10120-10125 (2007).
54 Alexeev, O. S., Chin, S. Y., Engelhard, M. H., Ortiz-Soto, L. & Amiridis, M. D. Effects of reduction temperature and metal-support interactions on the catalytic activity of Pt/gamma-Al_2O_3 and Pt/TiO_2 for the oxidation of CO in the presence and absence of H_2. *J. Phys. Chem. B* **109**, 23430-23443 (2005).
55 Lin, J. *et al.* Design of a highly active Ir/Fe$(OH)_x$ catalyst: versatile application of Pt-group metals for the preferential oxidation of carbon monoxide. *Angew. Chem. Int. Ed.* **51**, 2920-2924 (2012).
56 Liu, K. *et al.* Quasi In Situ Fe-57 Mossbauer Spectroscopic Study: Quantitative Correlation between Fe^{2+} and H_2 Concentration for PROX over Ir-Fe/SiO_2 Catalyst. *J. Phys. Chem. C* **114**, 8533-8541 (2010).
57 Scirè, S., Fiorenza, R., Gulino, A., Cristaldi, A. & Riccobene, P. M. Selective oxidation of CO in H_2-rich stream over ZSM5 zeolites supported Ru catalysts: An investigation on the role of the support and the Ru particle size. *Appl. Catal. A Gen.* **520**, 82-91 (2016).
58 Laguna, O. H., Romero Sarria, F., Centeno, M. A. & Odriozola, J. A. Gold supported on metal-doped ceria catalysts (M=Zr, Zn and Fe) for the preferential oxidation of CO (PROX). *J. Catal.* **276**, 360-370 (2010).
59 Qiao, B. T. *et al.* Highly Efficient Catalysis of Preferential Oxidation of CO in H-2-Rich Stream by Gold Single-Atom Catalysts. *ACS Catal.* **5**, 6249-6254 (2015).
60 Yi, G. *et al.* Preferential CO oxidation in a H_2-rich gas by Au/CeO_2 catalysts: Nanoscale CeO_2 shape effect and mechanism aspect. *Catal. Today* **157**, 83-88 (2010).
61 Ilieva, L. *et al.* Preferential oxidation of CO in H_2 rich stream (PROX) over gold catalysts supported on doped ceria: Effect of preparation method and nature of dopant. *Catal. Today* **158**, 44-55 (2010).
62 Wang, F. *et al.* In Situ EPR Study of the Redox Properties of CuO–CeO_2 Catalysts for Preferential CO Oxidation (PROX). *ACS Catal.* **6**, 3520-3530 (2016).
63 Caputo, T., Lisi, L., Pirone, R. & Russo, G. Kinetics of the preferential oxidation of CO over CuO/CeO_2 catalysts in H_2-rich gases. *Ind. Eng. Chem. Res.* **46**, 6793-6800 (2007).
64 Kim, D. H. & Cha, J. E. A CuO-CeO_2 mixed-oxide catalyst for CO clean-up by selective oxidation in hydrogen-rich mixtures. *Catal. Lett.* **86**, 107-112 (2003).
65 Avgouropoulos, G. & Ioannides, T. Effect of synthesis parameters on catalytic properties of CuO-CeO_2. *Appl. Catal. B Environ.* **67**, 1-11 (2006).
66 Chen, Y., Liaw, B., Chang, W. & Huang, C. Selective oxidation of CO in excess hydrogen over CuO/CexZr1-xO2–Al2O3CuO/CexZr1-xO2–Al2O3 catalysts. *Int. J. Hydrogen Energy* **32**, 4550-4558 (2007).
67 Moretti, E. *et al.* Catalytic purification of hydrogen streams by PROX on Cu supported on an organized mesoporous ceria-modified alumina. *Appl. Catal. B Environ.* **72**, 149-156 (2007).
68 Qiao, B. T. *et al.* Single-atom catalysis of CO oxidation using Pt_1/FeO_x. *Nat. Chem.* **3**, 634-641 (2011).
69 Tomaszewski, P. *Golden book of phase transitions*. Vol. 1 (2002).
70 Fjellvåg, H., Grønvold, F., Stølen, S. & Hauback, B. On the crystallographic and magnetic structures of nearly stoichiometric iron monoxide. *Journal of Solid State Chemistry* **124**, 52-57 (1996).
71 Maslen, E., Streltsov, V., Streltsova, N. & Ishizawa, N. Synchrotron X-ray study of the electron density in α-Fe2O3. *Acta Crystallographica Section B: Structural Science* **50**, 435-441 (1994).
72 Zhukhlistov, A. Crystal structure of lepidocrocite FeO (OH) from the electron-diffractometry data. *Crystallography Reports* **46**, 730-733 (2001).
73 Edwards, J. W., Speiser, R. & Johnston, H. L. High Temperature Structure and Thermal Expansion of Some Metals as Determined by X‐Ray Diffraction Data. I. Platinum, Tantalum, Niobium, and Molybdenum. *J. Appl. Phys.* **22**, 424-428 (1951).
74 Rao, U. V. *Platinum group metals and compounds*. (ACS Publications, 1971).